Journal of Computational Physics **159,** 377–406 (2000)
doi:10.1006/jcph.2000.6449, available online at http://www.idealibrary.com on IDEAL®

Development of Computational Aeroacoustics Equations for Subsonic Flows Using a Mach Number Expansion Approach

Scot A. Slimon,*,† Marios C. Soteriou,*,[1] and Donald W. Davis†

*University of Connecticut, Storrs, Connecticut 06269; and †Electric Boat Corporation, Groton, Connecticut 06340-4989

Received April 6, 1999; revised December 23, 1999

Computational aeroacoustics equations are developed using a Janzen–Rayleigh expansion of the compressible flow equations. Separate expansions are applied to an inner region characterized to lowest order by an incompressible flow field and an outer region characterized by propagating acoustic waves. Several perturbation equation sets are developed in the inner and outer regions by truncating the expanded equations using different orders in the perturbation variable, ε, where ε^2 is proportional to the square of the Mach number characterizing the flow. Composite equation sets are constructed by matching the equations governing the inner and outer regions. The highest-order perturbation continuity and momentum equations include an infinite series in ε^2 and are shown to be identical to the equations used in the expansion about incompressible flow approach. As such, the perturbation analysis is used to interpret the physical meaning of the perturbation variables and to highlight the assumptions inherent in this approach. Differences between numerical solutions obtained with the composite equation sets are evaluated for two unsteady flow problems. The lowest-order perturbation equation set is shown to yield adequate acoustic predictions for low Mach number flows. This equation set is considerably simpler to implement into a numerical solver and reduces the required CPU time relative to the highest-order equation set.

I. INTRODUCTION

The problem of predicting the sound generated by an unsteady flow field is one of significant practical interest. Computational aeroacoustics (CAA), which encompasses the application of computational methods to this problem, is emerging as a viable field due to advances in the speed and memory of high-performance computers. Despite these advances

[1]To whom correspondence should be addressed.

0021-9991/00 $35.00

there are several issues, distinct from those of the more mature field of computational fluid dynamics (CFD), that have limited the widespread application of CAA. These issues have been well documented for direct simulation (i.e., simultaneous computation of the near and far fields) of low Mach number (M) flows and are due, in part, to the disparity in scales associated with the near and far fields [1–3]. The near field has length scales that characterize the vortical flow, such as shear layer thickness or turbulent eddy size. These characteristic length scales are extremely small for moderate-to-high Reynolds number flows. The far field has length scales associated with the acoustic waves. For low frequencies and low Mach numbers, the far-field length scales can be many orders of magnitude larger than those characterizing the vortical flow. This wide variation in length scales directly affects the cost of direct simulation. A small near-field length scale requires the use of a small time step, whereas a large far-field length scale requires the use of a large computational domain. There is also large disparity in the amplitude of the near-field and far-field oscillations (e.g., the ratio of far-field to near-field kinetic energy fluctuations is on the order of M^4) [4]. Simultaneous resolution of these fields requires careful numerical treatment, such as the use of high-order numerical algorithms to minimize dispersion and dissipation error, and non-reflecting boundary conditions to reduce non-physical reflection from the computational boundaries.

The acoustic analogy provides a simplified approach that avoids the issues associated with direct simulation of low Mach number flow generated sound. In this approach, the governing equations are cast in the form of an inhomogeneous wave equation for a quantity (e.g., density) that becomes an acoustic fluctuation (e.g., acoustic density) in the far field. The inhomogeneity is generally considered the "source" of sound, which is non-zero in the near field. Several different forms of the acoustic analogy have been proposed to either provide different physical interpretation of the sources of sound or simplify the terms used to represent these sources [5–7]. For Lighthill's acoustic analogy [5], the wave equation takes the non-dimensional form

$$\frac{\partial^2 \rho}{\partial t^2} - \frac{1}{M^2}\frac{\partial^2 \rho}{\partial x_i \partial x_i} = \frac{\partial^2 T_{ij}}{\partial x_i \partial x_j} \tag{1}$$

with

$$T_{ij} = \rho u_i u_j + \delta_{ij}\left(p - \frac{1}{M^2}\rho\right) - \frac{1}{\mathrm{Re}}\tau_{ij}, \tag{2}$$

where ρ is the density, u_i, is the velocity vector, p is the pressure, τ_{ij} is the viscous stress tensor, t is time, x_i are the Cartesian coordinates, and Re is the Reynolds number. If T_{ij} is known, the solution to Eq. (1) can be determined using Green's functions [8]. For low Mach number flows, a common approximation is to assume $T_{ij} \approx T_{ij}^{(0)}$, where $T_{ij}^{(0)}$ is the stress tensor formed using the incompressible flow field (i.e., $T_{ij}^{(0)} = \rho_\infty u_{0i} u_{0j}$, where ρ_∞ is the ambient thermodynamic density, and u_{0i} is the incompressible velocity vector). The assumption to neglect the compressible portion of $\rho u_i u_j$ has been analyzed by Crow [9], who considered the following expansion of the right-hand side of Eq. (1),

$$\frac{\partial^2 T_{ij}}{\partial x_i \partial x_j} = \frac{\partial^2}{\partial x_i \partial x_j}\left(T_{ij}^{(0)} + M^2 T_{ij}^{(2)} + \cdots\right), \tag{3}$$

where ρ has been non-dimensionalized by ρ_∞. The second-order term $M^2 T_{ij}^{(2)}$ is of order M^2 smaller than $T_{ij}^{(0)}$ and is required to make the left- and right-hand sides of Eq. (1) consistent since $\partial^2 \rho / \partial t^2$ is of the same order. Despite this, Crow concluded that the approximation

$T_{ij} \approx T_{ij}^{(0)}$ is adequate for low Mach number, "uncomplicated" flows that do not contain extensive source regions. However, for flows with moderate-to-high Mach numbers, and for flows with acoustic source regions of the same order as or larger than the acoustic wavelength, the term $M^2 T_{ij}^{(2)}$ is important to the convection, refraction, and generation of the acoustic field. Modifications to Lighthill's acoustic analogy have been proposed in order to account for such effects. Lilley's [10] equation is one such modification that casts the wave operator in a form that reduces to that of the moving-medium wave equation. In this way, Lilley's equation accounts for the effects of convection and refraction. A general solution of Lilley's equation cannot be obtained through the use of Green's functions. Such solutions will typically require the use of numerical methods and are significantly more expensive to obtain relative to the solution of Eq. (1). More recently, Ristorcelli [11] has developed a modification to Lighthill's acoustic analogy in an attempt to account for sound generation due to compressible portions of $\rho u_i u_j$ (i.e., the $M^2 T_{ij}^{(2)}$ source term of Eq. (3)). The $M^2 T_{ij}^{(2)}$ source terms are determined directly from the incompressible flow field and do not account for the effects of the mean flow on convecting and refracting the acoustic field.

Hardin and Pope [12] have proposed a computational aeroacoustics technique that, similar to the acoustic analogy approach, avoids some of the issues and difficulties associated with direct simulation. This technique, called expansion about incompressible flow (EIF), is applicable to subsonic flows and uses acoustic source terms determined from the solution of the equations governing incompressible flow. In the EIF approach the velocity vector and pressure are split into incompressible and perturbation quantities, $u_i = u_{0i} + u_i'$ and $p = p_1 + p'$, where u_i' is the perturbation velocity vector, p_1 is the hydrodynamic pressure, and p' is the perturbation pressure. In addition, the density is split according to $\rho = \rho_0 + \rho_1 + \rho'$, where ρ_0 is the thermodynamic density, and ρ_1 is the hydrodynamic density, and ρ' is the perturbation density. The equations governing the acoustic field are developed by first substituting the split variables into the compressible flow equations, and then subtracting the incompressible flow equations. The resulting equations are

$$\frac{\partial \rho'}{\partial t} + \frac{\partial}{\partial x_i}[(\rho_0 + \rho_1 + \rho')u_i' + \rho' u_{0i}] = -\frac{\partial \rho_1}{\partial t} - u_{0i}\frac{\partial \rho_1}{\partial x_i} \tag{4a}$$

$$\frac{\partial}{\partial t}[(\rho_0 + \rho_1 + \rho')u_i' + \rho' u_{0i}] + \frac{\partial}{\partial x_j}[(\rho_0 + \rho_1)(u_{0i}u_j' + u_{0j}u_i' + u_i'u_j')]$$
$$+ \frac{\partial}{\partial x_j}[\rho'(u_{0i}u_{0j} + u_{0i}u_j' + u_{0j}u_i' + u_i'u_j')] + \frac{\partial p'}{\partial x_i} = -\frac{\partial(\rho_1 u_{0i})}{\partial t} - \frac{\partial(\rho_1 u_{0i}u_{0j})}{\partial x_j}. \tag{4b}$$

In the development of Eq. (4b), the effect of viscous action on the acoustic variables has been neglected. These equations have been written in such a way that only the acoustic source terms (i.e., terms that are constructed entirely from the incompressible flow solution) appear on the right-hand side of each equation. By splitting the flow field into incompressible and perturbation parts, and by neglecting the viscous terms in the acoustic equation, the EIF approach has been designed with the intent of accommodating the different discretization requirements resulting from the disparate length scales associated with low Mach number flows. The small vortical length scales are resolved by solving the incompressible flow equations on a hydrodynamic grid, and the large acoustic length scales are resolved by solving Eqs. (4a) and (4b) on a separate acoustic grid. In addition, the EIF approach allows for specification of different boundary condition types and locations for the near-field and

far-field quantities. One limitation of this approach is that it does not account for the effects of back scatter (i.e., acoustic feedback onto the underlying flow field).

Equations of state relating p_1 to ρ_1, and p' to ρ' and ρ_1, complete the EIF approach. The first of these relations is given by [12]

$$\rho_1 = \frac{1}{c_o^2}(p_1 - \tilde{p}_1), \tag{4c}$$

where

$$\tilde{p}_1 = \lim_{t\to\infty} \frac{1}{t} \int_0^t p_1(x_i, t)\, dt.$$

The rationale for subtracting out the time-averaged pressure, $\tilde{p}_1$, in computing ρ_1 is that the time-averaged pressure is primarily the result of non-isentropic effects and that these effects are slow relative to an acoustic time scale. For the second equation of state two different forms have been proposed [12]:

$$p' = c^2(\rho' + \rho_1) \tag{4d}$$

and

$$p' = p_0\left(\frac{\rho_0 + \rho_1 + \rho'}{\rho_0}\right)^{\gamma} - p_1. \tag{4e}$$

Equation (4d) has been used for a flow field with significant viscous effects [13], whereas Eq. (4e) has been used for inviscid flows [12, 14].

As described above, the EIF equations were developed by simply splitting the flow field into thermodynamic, incompressible, and acoustic parts. Because of this simple decomposition, the benefits and limitations of the approach, the inherent assumptions of the resulting set of equations, and the significance of the perturbation quantities in various regions of the flow are not clearly defined. In addition, Eqs. (4c) and (4d) were developed using a heuristic approach. In the present investigation, the EIF continuity and momentum equations are developed using a perturbation analysis. In a consistent fashion, new equations relating p_1 to ρ_1 and p' to ρ' and ρ_1, are also established. The perturbation analysis uses a Janzen–Rayleigh (i.e., Mach number squared) expansion about the thermodynamic field, extending the approach to include flows with significant heat release and/or heat conduction. This analysis will be shown to be valid in an inner region that is characterized to lowest order by the incompressible flow equations. Outside this region, the equations transition to a different set of equations that govern the propagation of acoustic waves. This transition is associated with the variation in scales associated with the inner and outer flow fields. Composite equations, valid over the entire flow field, are constructed using a technique analogous to the "additive composition" [15] method. These equations are applied in the numerical solution of the aeroacoustic fields associated with two unsteady flows.

II. ANALYSIS

The following analysis is performed in five sections, starting with an introduction of the governing equations in Section A. In Section B, a Janzen–Rayleigh expansion of the governing equations is used to develop a sequence of perturbation equation sets by equating terms of like order in the perturbation variable. In Sections C and D, a sequence of near-field

EIF equation sets and pressure–density relations are constructed from these perturbation equations. In Section E, the equations in Section C are rewritten in a form similar to that used in acoustic analogies. In addition, the uniformity of these equations is extended out to the far field by matching acoustic wave equations with the near-field EIF equations using a technique analogous to the additive composition matching method. In Section F, the developed equation sets are compared to Lighthill's acoustic analogy. In Section G, some numerical considerations of these equation sets are discussed.

A. *Governing Equations*

The generation and propagation of sound due to viscous flow are completely characterized by the compressible continuity, momentum and energy equations, and an equation of state,

$$\frac{\partial \rho}{\partial t} + \frac{\partial \rho u_i}{\partial x_i} = 0 \tag{5a}$$

$$\rho \frac{\partial u_i}{\partial t} + \rho u_j \frac{\partial u_i}{\partial x_j} = -\frac{1}{\gamma M^2} \frac{\partial p}{\partial x_i} + \frac{1}{\mathrm{Re}} \frac{\partial \tau_{ij}}{\partial x_j} + \rho F_i \tag{5b}$$

$$\frac{1}{\gamma M^2}\left[\rho \frac{\partial T}{\partial t} + \rho u_i \frac{\partial T}{\partial x_i}\right] = \frac{1}{\gamma M^2}\left[\frac{1}{\mathrm{Pr}\,\mathrm{Re}} \frac{\partial q_i}{\partial x_i} + q''' + \frac{(\gamma - 1)}{\gamma}\left(\frac{\partial p}{\partial t} + u_i \frac{\partial p}{\partial x_i}\right)\right] + \frac{(\gamma - 1)}{\mathrm{Re}} \Phi \tag{5c}$$

$$p = \rho T, \tag{5d}$$

where T is temperature, F_i is the body force per unit volume, Pr is the Prandtl number, γ is the specific heat ratio, Φ is the viscous dissipation function, q''' is heat release per unit volume, and q_i is the heat flux vector ($q_i = \partial(kT)/\partial x_i$). These equations have been developed assuming an ideal fluid with constant specific heat (c_p) and have been non-dimensionalized using u_∞, ρ_∞, L_∞, μ_∞, k_∞, and T_∞. Note that the energy equation, Eq. (5c), could have been simplified by multiplying each side by γM^2. However, Eq. (5c) provides a form convenient for perturbation analysis as discussed later in this paper.

B. *Janzen–Rayleigh Expansion*

The Janzen–Rayleigh expansion is an asymptotic perturbation analysis method that has been previously used to evaluate the effects of compressibility for certain flows [15]. It is performed by expanding each of the non-dimensionalized independent variables of Eqs. (5a)–(5d) in a power series in ε, where $\varepsilon^2 = \gamma M^2$,

$$\begin{aligned}
p &= p_0 + \varepsilon^2 \bar{p}_1 + \varepsilon^4 \bar{p}_2 + \varepsilon^6 \bar{p}_3 + \cdots = p_0 + p_1 + p_2 + p_3 + \cdots, \\
\rho &= \rho_0 + \varepsilon^2 \bar{\rho}_1 + \varepsilon^4 \bar{\rho}_2 + \varepsilon^6 \bar{\rho}_3 + \cdots = \rho_0 + \rho_1 + \rho_2 + \rho_3 + \cdots, \\
u_i &= u_{0i} + \varepsilon^2 \bar{u}_{1i} + \varepsilon^4 \bar{u}_{2i} + \varepsilon^6 \bar{u}_{3i} + \cdots = u_{0i} + u_{1i} + u_{2i} + u_{3i} + \cdots, \\
T &= T_0 + \varepsilon^2 \bar{T}_1 + \varepsilon^4 \bar{T}_2 + \varepsilon^6 \bar{T}_3 + \cdots = T_0 + T_1 + T_2 + T_3 + \cdots,
\end{aligned} \tag{6}$$

where $p_1 = \varepsilon^2 \bar{p}_1$, $p_2 = \varepsilon^4 \bar{p}_2$, etc. As seen in these expansions, the first-order correction is proportional to γM^2, with higher-order corrections using successive powers of γM^2. The basis of the Janzen–Rayleigh expansion is that a series of equations can be developed by substituting Eqs. (6) into the governing equations, Eqs. (5a)–(5d), and then grouping terms of like order in ε. The expansion is valid for arbitrary values of ε, so long as ε is less than unity

(i.e., the flow is subsonic). With this constraint, the expansion yields a convergent solution in the near field or inner region of the flow [15]. Substituting Eqs. (6) into Eqs. (5a)–(5d), and grouping terms of lowest order in ε (i.e., ε^{-2}) yields the "zeroth-order" approximation

$$\frac{\partial p_0}{\partial x_i} = 0 \tag{7a}$$

$$\rho_0 \frac{\partial T_0}{\partial t} + \rho_0 u_{0i} \frac{\partial T_0}{\partial x_i} = \frac{1}{\mathrm{Pr}\,\mathrm{Re}} \frac{\partial q_{0i}}{\partial x_i} + q''' + \frac{(\gamma - 1)}{\gamma} \frac{\partial p_0}{\partial t} \tag{7b}$$

$$\frac{p_0}{\rho_0} = T_0, \tag{7c}$$

where q_{0i} is constructed using gradients of T_0. Grouping terms of order ε^0 yields the "first-order" approximation

$$\frac{\partial \rho_0}{\partial t} + \frac{\partial \rho_0 u_{0i}}{\partial x_i} = 0 \tag{8a}$$

$$\rho_0 \frac{\partial u_{0i}}{\partial t} + \rho_0 u_{0j} \frac{\partial u_{0i}}{\partial x_j} = -\frac{1}{\gamma M^2} \frac{\partial p_1}{\partial x_i} + \frac{1}{\mathrm{Re}} \frac{\partial \tau_{0ij}}{\partial x_j} + \rho_0 F_i \tag{8b}$$

$$\begin{aligned} &\rho_0 \frac{\partial T_1}{\partial t} + \rho_0 u_{0i} \frac{\partial T_1}{\partial x_i} + \rho_1 \frac{\partial T_0}{\partial t} + (\rho_1 u_{0i} + \rho_0 u_{1i}) \frac{\partial T_0}{\partial x_i} \\ &\quad = \frac{1}{\mathrm{Pr}\,\mathrm{Re}} \frac{\partial^2 q_{1i}}{\partial x_i} + \frac{(\gamma - 1)}{\gamma} \left(\frac{\partial p_1}{\partial t} + u_{0i} \frac{\partial p_1}{\partial x_i} \right) + \frac{M^2 \gamma (\gamma - 1)}{\mathrm{Re}} \Phi_0 \end{aligned} \tag{8c}$$

$$\frac{p_1 - \rho_1 T_0}{\rho_0} = T_1, \tag{8d}$$

where Φ_0 and τ_{0ij} are constructed using gradients of u_{0i}, and q_{1i} is constructed using gradients of T_1. Grouping terms of order ε^2 yields the "second-order" approximation

$$\frac{\partial (\rho_0 u_{1i})}{\partial x_i} = -\frac{\partial \rho_1}{\partial t} - u_{0i} \frac{\partial \rho_1}{\partial x_i} \tag{9a}$$

$$\frac{\partial (\rho_0 u_{1i})}{\partial t} + \frac{\partial}{\partial x_j} [\rho_0 (u_{0i} u_{1j} + u_{0j} u_{1i})] + \frac{1}{\gamma M^2} \frac{\partial p_2}{\partial x_i} - \frac{1}{\mathrm{Re}} \frac{\partial \tau_{1ij}}{\partial x_j} = -\frac{\partial (\rho_1 u_{0i})}{\partial t} - \frac{\partial (\rho_1 u_{0i} u_{0j})}{\partial x_j} \tag{9b}$$

$$\begin{aligned} &\rho_0 \frac{\partial T_2}{\partial t} + \rho_1 \frac{\partial T_1}{\partial t} + \rho_0 u_{0i} \frac{\partial T_2}{\partial x_i} + \rho_1 u_{0i} \frac{\partial T_1}{\partial x_i} + (\rho_1 u_{1i} + \rho_0 u_{2i} + \rho_2 u_{0i}) \frac{\partial T_0}{\partial x_i} \\ &\quad = \frac{1}{\mathrm{Pr}\,\mathrm{Re}} \frac{\partial^2 q_{2i}}{\partial x_i} + \frac{(\gamma - 1)}{\gamma} \left(\frac{\partial p_2}{\partial t} + u_{0i} \frac{\partial p_2}{\partial x_i} + u_{1i} \frac{\partial p_1}{\partial x_i} + u_{2i} \frac{\partial p_0}{\partial x_i} \right) + \frac{M^2 \gamma (\gamma - 1)}{\mathrm{Re}} \Phi_1 \end{aligned} \tag{9c}$$

$$\frac{p_2 - \rho_1 T_1 - \rho_2 T_0}{\rho_0} = T_2, \tag{9d}$$

where Φ_1 and τ_{1ij} are constructed using gradients of u_{1i}, and q_{2i} is constructed using gradients of T_2. The zeroth-order approximation governs the thermodynamic field (p_0, ρ_0, T_0), the first-order approximation governs the hydrodynamic field (p_1, ρ_1, u_{0i}, T_1), and the second-order approximation governs an M^2 approximation of the perturbation (i.e., compressible) field (p_2, ρ_2, u_{1i}, T_2) for $M < 1$. Equations (7), (8), (9a), and (9b) represent a closed system. High values of ε (assuming $\varepsilon < 1$) will require higher-order expansions to accurately characterize the compressibility of the flow field. If one is interested in the temperature

fluctuations due to the near-field compressibility, or a higher-order approximation of the corresponding density and velocity field, Eqs. (9c) and (9d) and a "third-order" continuity and momentum equation of order ε^4 must be solved,

$$\frac{\partial \rho_2}{\partial t} + \frac{\partial(\rho_0 u_{2i} + \rho_1 u_{1i} + \rho_2 u_{0i})}{\partial x_i} = 0 \tag{10a}$$

$$\frac{\partial}{\partial t}[\rho_0 u_{2i} + \rho_1 u_{1i} + \rho_2 u_{0i}] + \frac{\partial}{\partial x_j}[\rho_0(u_{0i}u_{2j} + u_{0j}u_{2i} + u_{1i}u_{1j})] + \frac{\partial}{\partial x_j}[\rho_1(u_{0i}u_{1j} + u_{0j}u_{1i}) + \rho_2(u_{0i}u_{0j})] + \frac{1}{\gamma M^2}\frac{\partial p_3}{\partial x_i} - \frac{1}{\mathrm{Re}}\frac{\partial \tau_{2ij}}{\partial x_j} = 0. \tag{10b}$$

This process can be continued, yielding equations accurate to order ε^6, order ε^8, etc. Boundary conditions for these equations are obtained by substituting Eqs. (6) into the compressible flow boundary conditions. Although this yields a mathematically consistent problem, there is some difficulty in specifying boundary conditions for subsonic flows with moderate Mach numbers. The expanded form of these boundary conditions requires knowledge of both the incompressible and perturbation velocity fields. The latter is rarely known in practice.

C. *The Near-Field EIF Equations*

One of the goals of this investigation is to derive the equations in the EIF approach using a perturbation technique so as to better understand the underlying assumptions and limitations of this approach. This is accomplished by considering the case of a non-varying thermodynamic field (i.e., $p_0 = \rho_0 = T_0 = 1$) and by neglecting the viscous terms in all of the equations except the lowest remaining order (i.e., the hydrodynamic equations). Under these assumptions, the $\mathcal{O}(\varepsilon^0)$ inner region equations are obtained; that is, Eqs. (8a) and (8b) become

$$\frac{\partial u_{0i}}{\partial x_i} = 0 \tag{11a}$$

$$\frac{\partial u_{0i}}{\partial t} + u_{0j}\frac{\partial u_{0i}}{\partial x_j} = -\frac{1}{\gamma M^2}\frac{\partial p_1}{\partial x_i} + \frac{1}{\mathrm{Re}}\frac{\partial \tau_{0ij}}{\partial x_j} + F_i. \tag{11b}$$

These equations are recognized as the incompressible continuity and momentum equations. Simplified forms of the higher-order equations (e.g., Eqs. (9) and (10)) could be developed in a similar fashion. However, to obtain an order ε^4 or higher approximation of the near-field compressibility effects with such equations would be computationally cumbersome: The individual terms in the perturbation expansion would have to be solved using a series of equation sets, each with source terms developed from the solutions of lower-order equations in the series. A preferable approach would involve the solution of a single equation set for the entire pertubation field up to some order in ε. This would involve summing equation sets and is greatly aided by defining the perturbation quantities

$$\rho' = \sum_{m=2}^{n} \varepsilon^{2m}\,\overline{\rho}_m \tag{12a}$$

$$u_i' = \sum_{m=1}^{n} \varepsilon^{2m}\,\overline{u}_{mi} \tag{12b}$$

$$p' = \sum_{m=2}^{n} \varepsilon^{2m}\,\overline{p}_m, \tag{12c}$$

where the quantities ρ', u_i', p' represent an order ε^{2n} approximation of the entire density, velocity, and pressure perturbation fields, respectively. Using the perturbation quantities defined by Eqs. (12b) and (12c) with $n=1$, $\mathcal{O}(\varepsilon^2)$ inner region equations are obtained from simplified forms of Eqs. (9a) and (9b),

$$\frac{\partial u_i'}{\partial x_i} = -\frac{\partial \rho_1}{\partial t} - u_{0i}\frac{\partial \rho_1}{\partial x_i} \tag{13a}$$

$$\frac{\partial u_i'}{\partial t} + \frac{\partial (u_{0i}u_j' + u_{0j}u_i')}{\partial x_j} + \frac{1}{\gamma M^2}\frac{\partial p'}{\partial x_i} = -\frac{\partial (p_1 u_{0i})}{\partial t} - \frac{\partial (\rho_1 u_{0i}u_{0j})}{\partial x_j}. \tag{13b}$$

$\mathcal{O}(\varepsilon^4)$ inner region equations are obtained by combining Eqs. (9a) and (9b) with (10a) and (10b) and by using $n=2$ in Eqs. (12a)–(12c),

$$\frac{\partial \rho_2}{\partial t} + \frac{\partial}{\partial x_i}[(1+\rho_1)u_i' + \rho' u_{0i}] = -\frac{\partial \rho_1}{\partial t} - u_{0i}\frac{\partial \rho_1}{\partial x_i} \tag{14a}$$

$$\begin{aligned}&\frac{\partial}{\partial t}[(1+\rho_1)u_i' + \rho' u_{0i}] + \frac{\partial}{\partial x_j}[(1+\rho_1)(u_{0i}u_j' + u_{0j}u_i') + u_i'u_j'] \\ &\quad + \frac{\partial}{\partial x_j}[(\rho' u_{0i}u_{0j})] + \frac{1}{\gamma M^2}\frac{\partial p'}{\partial x_i} = -\frac{\partial (\rho_1 u_{0i})}{\partial t} - \frac{\partial (\rho_1 u_{0i}u_{0j})}{\partial x_j}.\end{aligned} \tag{14b}$$

The process used in developing these equations can be repeated indefinitely in extending the order of ε beyond that of Eqs. (14a) and (14b). If the entire series of higher-order equations (i.e., equations with terms of order ε^2, ε^4, ε^6, ε^8, etc.) are combined, the "baseline" inner region equations are obtained,

$$\frac{\partial \rho'}{\partial t} + \frac{\partial}{\partial x_i}[(1+\rho_1+\rho')u_i' + \rho' u_{0i}] = -\frac{\partial \rho_1}{\partial t} - u_{0i}\frac{\partial \rho_1}{\partial x_i} \tag{15a}$$

$$\begin{aligned}&\frac{\partial}{\partial t}[(1+\rho_1+\rho')u_i' + \rho' u_{0i}] + \frac{\partial}{\partial x_j}[(1+\rho_1)(u_{0i}u_j' + u_{0j}u_i' + u_i'u_j')] \\ &\quad + \frac{\partial}{\partial x_j}[\rho'(u_{0i}u_{0j} + u_{0i}u_j' + u_{0j}u_i' + u_i'u_j')] + \frac{1}{\gamma M^2}\frac{\partial p'}{\partial x_i} = -\frac{\partial (\rho_1 u_{0i})}{\partial t} - \frac{\partial (\rho_1 u_{0i}u_{0j})}{\partial x_j},\end{aligned} \tag{15b}$$

where $n=\infty$ has been used in Eqs. (12a)–(12c). The dimensional forms of Eqs. (15a) and (15b) are identical to the EIF acoustic continuity and momentum equations given by Eqs. (4a) and (4b). Since these equations include an infinite power series expansion in M^2, they are theoretically applicable to subsonic flows in the near field. Extending the applicability of the equations to include the outer, far-field region will be addressed later in this paper.

D. *Pressure–Density Relations*

The source terms shown on the right-hand side of Eqs. (13)–(15) are completely determined by solution of the incompressible flow equations and Eqs. (8c) and (8d). For constant ρ_0 and p_0, these latter equations can be combined into a pressure form of the

energy equation,

$$\frac{Dp_1}{Dt} - \gamma \frac{D\rho_1}{Dt} = \frac{1}{\mathrm{Pr\,Re}} \frac{\partial q_{1i}}{\partial x_i} + \frac{M^2 \gamma(\gamma - 1)}{\mathrm{Re}} \Phi_0. \tag{16a}$$

In an approach analogous to neglecting the viscous terms in the development of Eqs. (13)–(15), Eq. (16a) can be simplified by neglecting the diffusion terms,

$$\frac{Dp_1}{Dt} - \gamma \frac{D\rho_1}{Dt} = 0. \tag{16b}$$

Equation (16b) can be considered as the simple statement, $p_1 = \gamma \rho_1$. The dimensional form of this relation differs from the relation originally proposed for the EIF equations, Eq. (4c), since ρ_1 is related to the entire p_1 field, not just the unsteady component of this field (i.e., the time average of the hydrodynamic pressure is not subtracted out). It can be shown that time-averaged pressures are significant, even for isentropic flows (e.g., the classical acoustic problem of an oscillating sphere in an inviscid medium). These time-averaged pressures modify the unsteady source contributions due to unsteady hydrodynamic velocity fluctuations (e.g., the unsteady contributions due to $u_{0i}u_{0j}$ in the source term $\partial(\rho_1 u_{0i} u_{0j})/\partial x_j$ that appears in Eqs. (13b), (14b), and (15b)). Based on this, Eq. (16b) provides a more complete relation between p_1 and ρ_1. This result is advantageous since a time-averaged pressure need not be computed prior to computing the perturbation field. In addition to avoiding the extra effort associated with computing this pressure, Eq. (16b) allows the EIF approach to be used for transient flows (i.e., non-stationary flows in which a time-averaged hydrodyamic pressure field is not clearly defined).

Simplified equations for p' can be established in a similar fashion by combining the isentropic forms of Eqs. (9c) and (9d) with the higher-order energy equations and equations of state,

$$\frac{Dp'}{Dt} - \gamma \frac{D\rho'}{Dt} - \gamma \frac{D\Pi_n}{Dt} = 0, \tag{17}$$

where Π_n is order ε^n and is a non-linear function of ρ_1 and ρ' (e.g., $\Pi_4 = (\frac{\gamma-1}{2})\rho_1^2$, $\Pi_6 = \Pi_4 + (\frac{\gamma-1}{2})(\frac{\gamma-2}{3})\rho_1^3 + (\gamma - 1)\rho_1\rho'$, etc.), and the definitions of p' and ρ' are the same as the definitions used in Eqs. (13)–(15), depending on which equation set is being solved. Equation (17) is equivalent to an M^2-expansion of the isentropic relation $p = \rho^\gamma$ and can be solved along material lines assuming a quiescent initial field to yield $p' = \gamma(\rho' + \Pi_n)$. Numerical testing using the baseline EIF equations, and separately using Eqs. (4d) and (17), has shown that Eq. (17) provides the correct relationship between p', ρ', and ρ_1, given the stated assumptions.

E. *Extension to the Far Field: The Composite EIF Equations*

As described previously by several investigators [9, 16, 17], the aeroacoustic problem consists of two primary length scales: an "inner" length scale associated with the incompressible flow field (e.g., the size of a turbulent eddy, ℓ) and in "outer" length scale, λ, associated with propagating acoustic waves. In addition to the inner and outer length scales, Crow [9] describes a third relevant length scale, Λ, associated with the extent of the source region. If Λ is of the same order as λ, the source region is considered non-compact and can

interact with the acoustic field resulting in convection and refraction effects. These effects will be described in more detail later in this paper. The inner and outer length scales are related to each other such that $\ell/\lambda \sim M$, while the relevant velocity scales in the inner and outer regions are related by $u_\infty \sim Mc_o$. If the governing equations are non-dimensionalized using the outer region scales, the process of expanding each of the variables and equating like powers of ε results in a *different* set of equations relative to those developed using the Janzen–Rayleigh expansion in the inner region. As such, the inner region equations are not uniformly valid over the entire flow field. The matched asymptotic expansion (MAE) approach [15] is a singular perturbation method that has been used to address this issue. In this approach, separate equations are developed for the inner and outer regions. The outer region is governed by wave equations for $\hat{\rho}_2$, $\hat{\rho}_3$, $\hat{\rho}_4$, etc., where $\hat{\rho}_n$ is the nth term in an outer region expansion. The inner region is governed by the equations developed using the Janzen–Rayleigh expansion. Separate solutions are obtained for the equations governing the inner and outer regions. The harmonic functions in these separate solutions are then matched in some "intermediate" region based on the order of ε of each function. In this way, a composite solution can be constructed that is asymptotically valid over the entire flow domain.

The non-uniformity of the equations developed using the Janzen–Rayleigh expansion can be best illustrated by first considering acoustic analogy formulations of the $\mathcal{O}(\varepsilon^0)$-, $\mathcal{O}(\varepsilon^2)$-, $\mathcal{O}(\varepsilon^4)$-, and baseline EIF inner region equations. These formulations, which will also be used to facilitate the development of the composite EIF equations, can be developed by subtracting the time derivative of the perturbation continuity equation from the divergence of the perturbation momentum equation. Equation (17) can then be used to eliminate p',

$$-\frac{1}{M^2}\frac{\partial^2 \rho_1}{\partial x_i \partial x_i} = \frac{\partial^2 (u_{0i} u_{0j})}{\partial x_i \partial x_j} \tag{18}$$

$$-\frac{1}{M^2}\frac{\partial^2 \rho'}{\partial x_i \partial x_i} - \frac{\partial^2}{\partial x_i \partial x_j}[(u_{0i} u'_j + u_{0j} u'_i)] = -\frac{\partial^2 \rho_1}{\partial t^2} + \frac{1}{M^2}\frac{\partial^2 \Pi_4}{\partial x_i \partial x_i} + \frac{\partial^2 (\rho_1 u_{0i} u_{0j})}{\partial x_i \partial x_j} \tag{19}$$

$$\frac{\partial^2 \rho_2}{\partial t^2} - \frac{1}{M^2}\frac{\partial^2 \rho'}{\partial x_i \partial x_i} - \frac{\partial^2}{\partial x_i \partial x_j}[(1+\rho_1)(u_{0i} u'_j + u_{0j} u'_i) + u'_i u'_j + \rho' u_{0i} u_{0j})$$
$$= -\frac{\partial^2 \rho_1}{\partial t^2} + \frac{1}{M^2}\frac{\partial^2 \Pi_6}{\partial x_i \partial x_i} + \frac{\partial^2 (\rho_1 u_{0i} u_{0j})}{\partial x_i \partial x_j} \tag{20}$$

$$\frac{\partial^2 \rho'}{\partial t^2} - \frac{1}{M^2}\frac{\partial^2 \rho'}{\partial x_i \partial x_i} - \frac{\partial^2}{\partial x_i \partial x_j}[(1+\rho_1+\rho')(u_{0i} u'_j + u_{0j} u'_i + u'_i u'_j) + \rho' u_{0i} u_{0j}]$$
$$= -\frac{\partial^2 \rho_1}{\partial t^2} + \frac{1}{M^2}\frac{\partial^2 \Pi_\infty}{\partial x_i \partial x_i} + \frac{\partial^2 (\rho_1 u_{0i} u_{0j})}{\partial x_i \partial x_j}, \tag{21}$$

where Eq. (18) has been developed from Eqs. (11a) and (11b), and Eqs. (19)–(21) have been developed from Eqs. (13)–(15), respectively. The primed quantities in each of these acoustic analogy formulations are consistent with the definitions used in developing Eqs. (13)–(15).

To develop outer region equations analogous to Eqs. (18)–(21), a separate outer region expansion of each dependent variable is constructed. For example, the density in the outer region is expanded using $\rho = 1 + \Delta(\varepsilon^n)(\varepsilon^2 \hat{\rho}_2 + \varepsilon^4 \hat{\rho}_3 + \varepsilon^6 \hat{\rho}_4 + \cdots) = 1 + \hat{\rho}_2 + \hat{\rho}_3 + \hat{\rho}_4 + \cdots$, where $\Delta(\varepsilon^n)$ is a gauge function determined through the matching of

the inner and outer solutions. Similarly, the velocity field is expanded using $u_i = \hat{u}_{0i} + \hat{u}_{1i} + \hat{u}_{2i} + \hat{u}_{3i} + \cdots$. The sequence for velocity in the outer region is shifted by M relative to that in the inner region ($\hat{u}_{ni} = Mu_{ni}$) since the velocity field has been non-dimensionalized using the outer region velocity scale. The dimensional form of the first term in the velocity expansion is equivalent to the hydrodynamic velocity, u_{0i}. This quantity is uniform in the far field (i.e., its gradients are zero) such that there are no far-field density gradients resulting from $\hat{u}_{0i}$. This is consistent with the results of previous MAE investigations [17] in which the sequence for the higher-order density terms in the outer region has been shown to be shifted by ε^2 relative to that of the inner region (i.e., $\Delta(\varepsilon^n) = \varepsilon^2$, such that the second term in the outer expansion of density, $\hat{\rho}_2$, is order ε^4 in the inner region). Using this result, we can construct an outer region acoustic analogy equation analogous to the inner region $\mathcal{O}(\varepsilon^2)$-equation (Eq. (19)) as

$$\frac{\partial^2 \hat{\rho}_2}{\partial \hat{t}^2} - \frac{\partial^2 \hat{\rho}_2}{\partial \hat{x}_i \partial \hat{x}_i} = \frac{\partial^2 (\hat{u}_{0i}\hat{u}_{1j} + \hat{u}_{1i}\hat{u}_{0j})}{\partial \hat{x}_i \partial \hat{x}_j}. \tag{22}$$

In Eq. (22), the independent variables, $\hat{x}_i$ and $\hat{t}$ have been non-dimensionalized using the outer length and velocity scales. This equation can be rewritten using the inner-region-dependent variables as an $\mathcal{O}(\varepsilon^4)$-equation,

$$\frac{\partial^2 \rho_2}{\partial \hat{t}^2} - \frac{\partial^2 \rho_2}{\partial \hat{x}_i \partial \hat{x}_i} - M^2 \frac{\partial^2 (u_{0i}u_{1j} + u_{1i}u_{0j})}{\partial \hat{x}_i \partial \hat{x}_j} = 0. \tag{23}$$

As the relevant length and velocity scales transition from $\mathcal{O}(\ell)$ to $\mathcal{O}(\lambda)$, Eq. (19) transitions to Eq. (23). These equations are similar to the inner and outer equations used by Crow in his MAE analysis. By comparing the inner and outer region equations, it can be seen that Eq. (19) is not uniformly valid over the entire flow field. The term $\partial^2 \rho_2 / \partial t^2$ has been excluded in Eq. (19), whereas the entire right-hand side of Eq. (19) has been excluded in Eq. (23). These terms are ultimately responsible for the proper matching of the inner and outer solutions. If the analysis is not carried further than the order of ε resolved by Eqs. (19) and (23), then order ε^4 terms can be added to the $\mathcal{O}(\varepsilon^2)$ inner region equation without affecting the accuracy of this equation,

$$\frac{\partial^2 \rho'}{\partial t^2} - \frac{1}{M^2}\frac{\partial^2 \rho'}{\partial x_i \partial x_i} - \frac{\partial^2}{\partial x_i \partial x_j}[(u_{0i}u'_j + u_{0j}u'_i)] = -\frac{\partial^2 \rho_1}{\partial t^2} + \frac{1}{M^2}\frac{\partial^2 \Pi_4}{\partial x_i \partial x_i} + \frac{\partial^2 (\rho_1 u_{0i} u_{0j})}{\partial x_i \partial x_j}. \tag{24}$$

The development of Eq. (24) is similar to the additive composition method described by Van Dyke [15]. In this method, the composite expansion is constructed by summing the inner and outer solutions. This sum is then corrected by subtracting the part that these solutions have in common. In the development of Eq. (24), this corresponds to subtracting the quantities

$$-\frac{1}{M^2}\,\partial^2 \rho' / \partial x_i \partial x_i \qquad \text{and} \qquad -\partial^2 (u_{0i}u_{1j} + u_{1i}u_{0j}) / \partial x_i \partial x_j$$

from the sum of Eqs. (19) and (23). The principal difference between the additive composition method and that used in the current investigation is that the equations, as opposed to the corresponding solutions, have been matched.

The process used in developing Eq. (24) can also be used to develop composite forms of Eqs. (20) and (21),

$$\frac{\partial^2\rho'}{\partial t^2} - \frac{1}{M^2}\frac{\partial^2\rho'}{\partial x_i\partial x_i} - \frac{\partial^2}{\partial x_i\partial x_j}[(1+\rho_1)(u_{0i}u_j' + u_{0j}u_i') + u_i'u_j' + \rho' u_{0i}u_{0j}]$$
$$= -\frac{\partial^2\rho_1}{\partial t^2} + \frac{1}{M^2}\frac{\partial^2\Pi_6}{\partial x_i\partial x_i} + \frac{\partial^2(\rho_1 u_{0i}u_{0j})}{\partial x_i\partial x_j} \tag{25}$$

$$\frac{\partial^2\rho'}{\partial t^2} - \frac{1}{M^2}\frac{\partial^2\rho'}{\partial x_i\partial x_i} - \frac{\partial^2}{\partial x_i\partial x_j}[(1+\rho_1+\rho')(u_{0i}u_j' + u_{0j}u_i' + u_i'u_j') + \rho' u_{0i}u_{0j}]$$
$$= -\frac{\partial^2\rho_1}{\partial t^2} + \frac{1}{M^2}\frac{\partial^2\Pi_\infty}{\partial x_i\partial x_i} + \frac{\partial^2(\rho_1 u_{0i}u_{0j})}{\partial x_i\partial x_j}. \tag{26}$$

Equations (24)–(26) are composite equations with the same inner region order of ε accuracy as Eqs. (19)–(21). The source terms in these equations are identical to each other since they are of order ε^2. Thus, differences between the acoustic analogy formulations of the $\mathcal{O}(\varepsilon^2)$-, $\mathcal{O}(\varepsilon^4)$-, and baseline composite EIF equations are only seen in the flow–acoustic interaction terms (i.e., the third term on the left-hand side of each equation). The solution of Eqs. (24)–(26) can be loosely considered as a matched singular perturbation solution, using the nomenclature of Refs. [9, 16, 17], since the actual matching is performed on the equations as opposed to the solutions.

A procedure similar to that used to develop Eqs. (24)–(26) can be used to develop composite forms of the continuity and momentum equations. This involves the addition of time derivatives of order ε^{n+2} density terms to the $\mathcal{O}(\varepsilon^n)$ inner region continuity equation, as shown below:

$\mathcal{O}(\varepsilon^2)$ Composite EIF Equations $\mathcal{O}(\varepsilon^2)$ Inner Region, $\mathcal{O}(\varepsilon^4)$ Outer Region

$$\frac{\partial\rho'}{\partial t} + \frac{\partial u_i'}{\partial x_i} = -\frac{\partial\rho_1}{\partial t} - u_{0i}\frac{\partial\rho_1}{\partial x_i} \tag{27a}$$

$$\frac{\partial u_i'}{\partial t} + \frac{\partial(u_{0i}u_j' + u_{0j}u_i')}{\partial x_j} + \frac{1}{\gamma M^2}\frac{\partial p'}{\partial x_i} = -\frac{(\partial\rho_1 u_{0i})}{\partial t} - \frac{\partial(\rho_1 u_{0i}u_{0j})}{\partial x_j}. \tag{27b}$$

$\mathcal{O}(\varepsilon^4)$ Composite EIF Equations $\mathcal{O}(\varepsilon^4)$ Inner Region, $\mathcal{O}(\varepsilon^6)$ Outer Region

$$\frac{\partial\rho'}{\partial t} + \frac{\partial}{\partial x_i}[(1+\rho_1)u_i' + \rho' u_{0i}] = -\frac{\partial\rho_1}{\partial t} - u_{0i}\frac{\partial\rho_1}{\partial x_i} \tag{28a}$$

$$\frac{\partial}{\partial t}[(1+\rho_1)u_i' + \rho' u_{0i}] + \frac{\partial}{\partial x_j}[(1+\rho_1)(u_{0i}u_j' + u_{0j}u_i') + u_i'u_j']$$
$$+ \frac{\partial}{\partial x_j}[\rho' u_{0i}u_{0j}] + \frac{1}{\gamma M^2}\frac{\partial p'}{\partial x_i} = -\frac{\partial(\rho_1 u_{0i})}{\partial t} - \frac{\partial(\rho_1 u_{0i}u_{0j})}{\partial x_j}. \tag{28b}$$

Baseline Composite EIF Equations $\mathcal{O}(\varepsilon^\infty)$ Inner Region, $\mathcal{O}(\varepsilon^\infty)$ Outer Region

$$\frac{\partial\rho'}{\partial t} + \frac{\partial}{\partial x_i}[(1+\rho_1+\rho')u_i' + \rho' u_{0i}] = -\frac{\partial\rho_1}{\partial t} - u_{0i}\frac{\partial\rho_1}{\partial x_i} \tag{29a}$$

$$\frac{\partial}{\partial t}[(1+\rho_1+\rho')u_i' + \rho' u_{0i}] + \frac{\partial}{\partial x_j}[(1+\rho_1)(u_{0i}u_j' + u_{0j}u_i' + u_i'u_j')]$$
$$+ \frac{\partial}{\partial x_j}[\rho'(u_{0i}u_{0j} + u_{0i}u_j' + u_{0j}u_i' + u_i'u_j')] + \frac{1}{\gamma M^2}\frac{\partial p'}{\partial x_i} = -\frac{\partial(\rho_1 u_{0i})}{\partial t} - \frac{\partial(\rho_1 u_{0i}u_{0j})}{\partial x_j}. \tag{29b}$$

Note that the form of the inner region and composite equations are identical for the $\mathcal{O}(\varepsilon^4)$ and baseline cases. Although the form is identical, the definition of ρ' used in the composite equations provides the correct interpretation of ρ' in the outer region.

Even though the baseline EIF equations can be constructed to include an infinite power series in ε, solutions obtained with these equations can only be considered approximate. The approximation stems from the fact that the outer region equations are not matched with the $\mathcal{O}(\varepsilon^0)$-inner region equations. For example, if the procedure used to develop Eqs. (24)–(26) is followed in matching Eqs. (18) and (23), the following composite equations can be developed:

$\mathcal{O}(\varepsilon^0)$ Composite Equations $\mathcal{O}(\varepsilon^0)$ Inner Region, $\mathcal{O}(\varepsilon^2)$ Outer region

$$\frac{\partial \rho'}{\partial t} + \frac{\partial u_{0i}}{\partial x_i} = 0 \tag{30a}$$

$$\frac{\partial u_{0i}}{\partial t} + u_{0j}\frac{\partial u_{0i}}{\partial x_j} = -\frac{1}{\gamma M^2}\frac{\partial(p_1+p')}{\partial x_i} + \frac{1}{\mathrm{Re}}\frac{\partial \tau_{0ij}}{\partial x_j} + F_i. \tag{30b}$$

Equations (30a) and (30b) have been used in low Mach number acoustic simulations by Reitsma [18], who referred to them as the finite compressibility equations. Note that the acoustic field is coupled to the incompressible field such that u_{0i} is no longer solenoidal. As a result, ρ' consists of a more extensive density field than implied by Eq. (23); i.e., it inherently includes ρ_1. These equations highlight an approximation implicit in the use of Eqs. (24)–(26): The perturbation field has no interaction with the incompressible flow equations (i.e., acoustic back scatter effects are neglected). Therefore, the EIF equations should only be used to simulate aeroacoustic fields when these effects are negligible. Note that this is also a limitation of the MAE approach.

F. *Comparison with Lighthill's Acoustic Analogy*

The acoustic analogy formulations given by Eqs. (24)–(26) can be written in a form more consistent with Lighthill's acoustic analogy, Eq. (1), by using Eq. (18) and the relation $\rho = 1 + \rho_1 + \rho'$. This is performed below for Eq. (26):

$$\frac{\partial^2 \rho}{\partial t^2} - \frac{1}{M^2}\frac{\partial^2 \rho}{\partial x_i \partial x_i} - \frac{\partial^2}{\partial x_i \partial x_j}[\rho(u_{0i}u_j' + u_{0j}u_i' + u_i'u_j') + \rho' u_{0i}u_{0j}]$$
$$= \frac{1}{M^2}\frac{\partial^2 \Pi_\infty}{\partial x_i \partial x_i} + \frac{\partial^2(u_{0i}u_{0j})}{\partial x_i \partial x_j} + \frac{\partial^2 \rho_1(u_{0i}u_{0j})}{\partial x_i \partial x_j}. \tag{31}$$

The most significant difference between this equation and Eq. (1) is that flow–acoustic interaction terms have been separated from the sound generation process. Separation of

these terms is strictly dictated by the perturbation analysis. This contrasts with the somewhat ad hoc separation of these terms in other approaches such as in the development of Lilley's equation. The first term on the right-hand side of Eq. (31), $(1/M^2)\partial^2\Pi_\infty/\partial x_i\partial x_i)$, is equivalent to the $\delta_{ij}(p-(1/M^2)p)$ contribution in the Eq. (1) source term. The last term on the right-hand side of Eq. (31), which includes the hydrodynamic density (ρ_1), is similar to Term I of the following compressible "correction" (T_{ij}^c) posed by Ristorcelli [11]:

$$\frac{\partial^2 T_{ij}^c}{\partial x_i \partial x_j} = \underbrace{\frac{\partial^2 \rho_1 u_{0i} u_{0j}}{\partial x_i \partial x_j}}_{\text{Term I}} - \underbrace{2\frac{\partial}{\partial x_j}\left(u_{0j}\frac{D\rho_1}{Dt}\right)}_{\text{Term II}}. \tag{32}$$

The second compressible correction term, Term II, was derived from the irrotational component of the fluid–acoustic interaction term (i.e., the third term on the left-hand side of Eq. (31)) in an attempt to account for convection and refraction effects. The effects of the flow-acoustic interaction terms in the composite EIF equations, as well as the first compressible correction term (Term I in Eq. (32)) are evaluated under Numerical Results.

G. *Resolution of Disparate Acoustic and Convective Length Scales: Numerical Considerations*

One of the advantages of the EIF approach cited in the Introduction is that the technique accommodates the disparate length scales (i.e., acoustic and convective) associated with low Mach number aerodynamically generated sound. The smallest convective length scales are resolved on a hydrodynamic grid, while the acoustic length scales are resolved on a separate acoustic grid. Unfortunately, the hydrodynamic and acoustic grid spacing requirements are not independent from one another since the acoustic grid must accurately resolve the relevant convective length scales characterizing the source terms associated with the acoustic wavelengths of interest. For some problems this would require that the acoustic grid spacing be the same as or similar to that used in the hydrodynamic grid. However, for many flows the smallest scale hydrodynamic fluctuations are negligible contributors to the overall radiated sound field, even though these scales may be important to the development of the hydrodynamic flow field. For such flows, it may be possible to use an acoustic grid with coarser spacing relative to that used in the hydrodynamic grid.

Although the small-scale hydrodynamic fluctuations may be physically unimportant to the overall radiated sound, the numerical interpolation of these small scales from a fine hydrodynamic grid onto a coarse acoustic grid could result in errors in the magnitude and distribution of the acoustic source field. One approach used in the current investigation to help reduce such errors is to construct the acoustic source terms with their associated gradients on the hydrodynamic grid and to then interpolate these terms onto the acoustic grid. This reduces the discretization error relative to the alternate approach of interpolating the incompressible flow primitive variables onto the acoustic grid and computing the source terms using the same level of discretization provided by the acoustic grid spacing. Aliasing error associated with using different grid resolutions in the hydrodynamic and acoustic solutions depends on the magnitude of the acoustic sources arising from hydrodynamic scales that are not resolved by the acoustic grid. For some problems, such as the sound generation and radiation due to fine grain turbulence, this error may be difficult to assess and low-pass filtering of the acoustic source field may ultimately be required before this

field is interpolated onto the acoustic grid. In the current investigation (see Section III), the simulated flow fields were resolved using both simple analytical models and dissipative numerical methods such that the resulting hydrodynamic fields are not characterized by a large range in wavenumbers. The acoustic grids used in these simulations were designed to resolve this entire range. This reduced interpolation errors to acceptable levels as confirmed by a grid refinement study.

III. NUMERICAL RESULTS

A. *Baseline Composite EIF Equations*

The baseline composite EIF equations, Eqs. (29), along with the appropriate pressure–density relations, have been implemented into a CAA solver using a second-order MacCormack [19] scheme with a generalized body-fitted coordinate system. Radiation to the far field is treated using a perfectly matched layer [20, 21] (PML) non-reflecting boundary condition. The source terms that appear in the composite EIF equations are computed on the grid used for the incompressible flow solution and interpolated in space onto the acoustic grid using bilinear interpolation functions. Previous grid refinement studies [22] showed that 20 points per wavelength is required with the MacCormack scheme. In this paper, a minimum of 25 points per wavelength is used in all of the reported simulations. The incompressible Navier–Stokes flow solver [23, 24] used in this investigation is finite difference based (central spatial differencing and full non-orthogonal viscous terms) and uses a Briley–MacDonald linearized block, alternating direction implicit scheme. The governing equations are cast in primitive variable form in curvilinear coordinates, using a pseudo-compressibility term in the continuity equation to efficiently link the updates of the velocity and pressure fields. Time-accurate solutions are obtained with the incompressible flow solver using a subiteration approach [25], which extends the pseudo-compressibility method to time-accurate incompressible flows by subiterating each physical time step to drive the divergence of velocity to zero.

The CAA solver has been applied to several fundamental problems including sound generated due to a spinning vortex pair and a forced planar shear layer [22]. The basic configuration for the spinning vortex pair is shown in Fig. 1. The vortices have a characteristic rotating Mach number defined as $M_r = r_o\omega/c_o$, where r_o is the radius at which the vortices rotate about some origin, and ω is the angular velocity of this rotation. The angular velocity is related to r_o and the vortex circulation (Γ) by $\omega = \Gamma/4\pi r_o^2$. For the spinning vortex pair problem, the source terms used in the EIF equations were determined analytically from the inner (hydrodynamic) portion of an MAE solution [26]. An acoustic solution was obtained on a rectangular domain using a uniform grid with 78,961 uniformly spaced grid points ($\Delta x_i = 2r_o$). The acoustic solution, which is shown in Figs. 1b and 1c, was computed for 10 periods (i.e., 10 revolutions of the vortex pair) using $\Delta t = 0.0041$, $M_r = 0.05$, and $\Gamma = 0.2\pi$. Note the grid spacing used in the solution may appear to be insufficient in resolving the relevant near-field source terms. However, it can be shown that the relevant source term length scale is the length scale describing the hydrodynamic pressure variation. This scale is adequately resolved with $\Delta x_i = 2r_o$ and was verified by performing a grid sensitivity study [22, 27]. For grid spacings less than $\Delta x_i = 3r_o$ the solution was shown to be grid independent. The solution shown in Fig. 1c is seen to be in good agreement with the outer (acoustic) portion of the MAE solution, at least for $r_o > 40$. Some differences are seen near the vortex

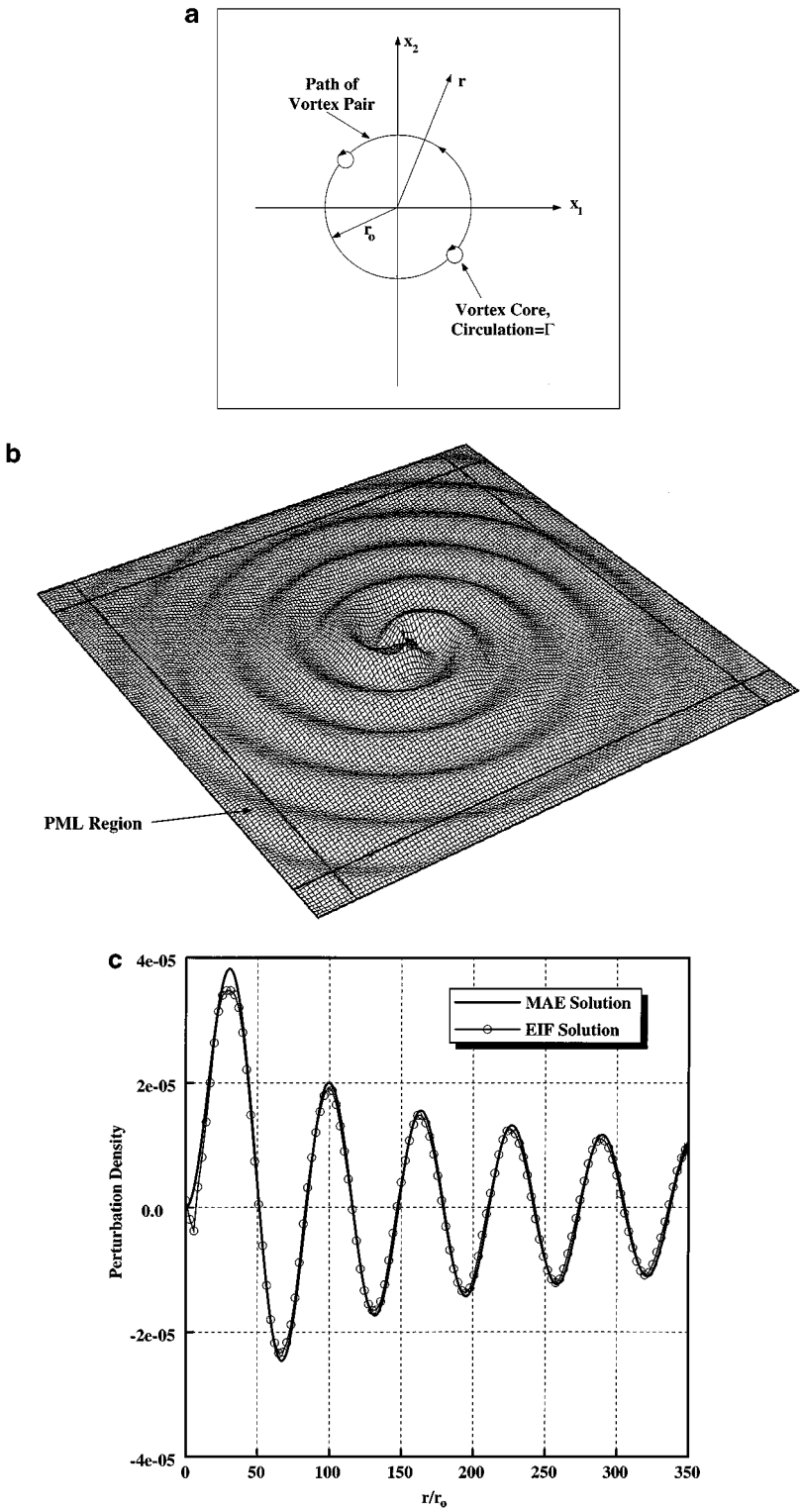

FIG. 1. Spinning vortex pair. (a) Configuration. (b) Acoustic density field. The computational grid (every other grid point shown for clarity) is deformed 2×10^3 times the acoustic density field, which ranges between -4×10^{-5} and 4×10^{-5}; dark lines outline the PML region. (c) Comparison of computed and MAE predicted acoustic pressure for $M_r = 0.05$.

cores ($r_o < 10$) and near the first peak in the acoustic field ($r_o = 30$). These differences are due to three principal reasons. First, the MAE solution only includes quadrupole terms (i.e., higher-order effects such as those due to octupole terms were excluded in the MAE analysis). These higher-order terms are inherently included in the EIF approach. Second, the MAE solution was obtained using linearized acoustic equations in the outer region, such that only the first terms in the outer expansion used in the current investigation were considered. In addition, the MAE solution does not account for flow–acoustic interaction effects. This point will be addressed in more detail in part B of this section. Third, the EIF solution represents a combination of near-field compressibility and acoustic waves. This fact is evident by the matching procedure performed between the near-field EIF equations and the outer region wave equations in the previous section. In contrast, the MAE solution contains only the acoustic component of pressure. The near-field compressibility effects were evaluated by solving Eqs. (13a) and (13b) for ρ'. Note that Eq. (13a) does not include a time derivative of ρ', such that the resulting solution does not propagate as acoustic waves. Significant compressibility effects were seen out to $r_o = 20$, accounting for some of the differences between the EIF and MAE solutions seen in this region.

Relevant flow features and computed acoustic pressure contours for the forced planar shear layer are shown in Fig. 2. For this flow, the hydrodynamic source terms were computed using an incompressible Navier–Stokes solver [23, 24] at $\mathrm{Re} = \rho_\infty \Delta u \delta/\mu = 250$, where δ is the shear layer thickness at the inlet given by $\delta = \Delta u/|\partial u_1/\partial x_2|_{\max}$, and Δu is the velocity difference across the shear layer. The perturbation solution was computed using a high-speed Mach number (M_{HS}) of 0.50 and a low-speed Mach number (M_{LS}) of 0.25. The hydrodynamic grid used in the incompressible flow solution extended approximately 500δ in the x_1 direction and 15δ in the x_2 direction. This grid had 117,530 points (730×161) and was clustered toward the shear layer centerline ($x_2 = 0$) with a minimum spacing of 0.04δ. The hydrodynamic inlet velocity was specified using an error function profile given by $u_1(x_2, t) = (u_{\mathrm{avg}}/2) + (\Delta u/2)[\mathrm{erf}(x_2/\sigma)]$, where u_{avg} is the average of the high- and low-speed stream velocities. Forcing was applied at the fundamental and first subharmonic frequencies using sine functions with an amplitude of $0.0002\Delta u$. This amplitude was just high enough to get the shear layer to roll up and overcome the dissipation inherent in the numerical scheme. A low level of forcing was selected to minimize the resulting noise source at the hydrodynamic inlet, and as a result the hydrodynamie field appears somewhat diffusive. The acoustic domain was designed such that the computational grid extended five wavelengths at the subharmonic frequency above and below the hydrodynamic grid. A uniform grid with 80,571 grid points and a spacing of $\Delta x_i = 0.145\delta$ was used. This provided sufficient resolution (approximately 15 grid points) of the pressure field associated with each subharmonic vortex. The source terms and unsteady components of each incompressible flow variable used in the acoustic solution were gradually decayed between $x_1/\delta = 145$ and $x_1/\delta = 220$ using a linear decay function. These variables were also decayed near the inlet to reduce the effects of forcing on the acoustic solution. Several variations of the downstream decay (e.g., different decay lengths, location of decay, and exponential decay functions) were used in computing the acoustic solution. These variations, which were shown to have no significant effect on the far-field solution, demonstrated that the decay region did not act as a source of sound. A highly directive acoustic field was predicted with a peak directivity near 30° below the centerline of the shear layer. This acoustic field has been shown [22] to be in good agreement with results obtained from DNS computations [28].

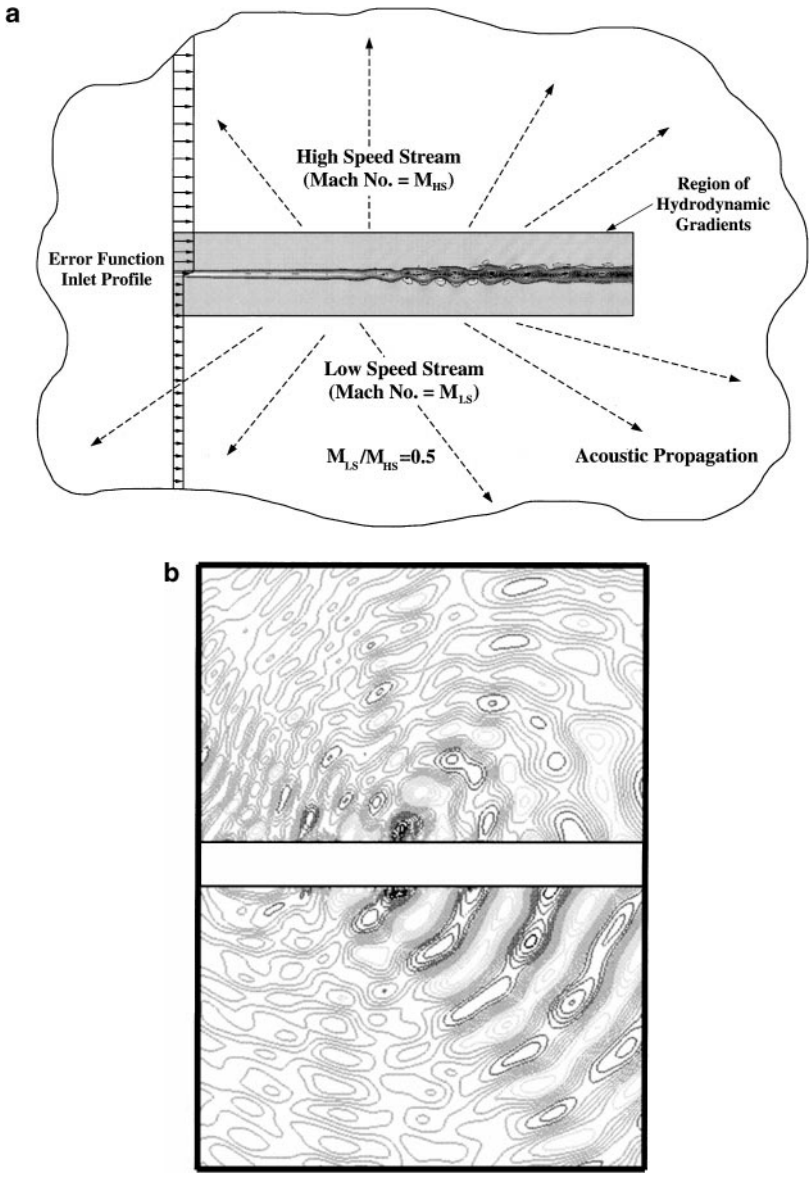

FIG. 2. Planar shear layer. (a) Vorticity contours. Contours range between -0.25 and 0.25; dark shading represents regions of high vorticity, contour lines are inverted to highlight vorticity field (light contour lines indicate high vorticity). (b) Dilatation field for $M_{\mathrm{HS}} = 0.50$ case. Contour levels range between -3.0×10^{-7} and 3.0×10^{-7} at intervals of 3.0×10^{-8}.

B. *Comparison of $\mathcal{O}(\varepsilon^2)$-, $\mathcal{O}(\varepsilon^4)$-, and Baseline Composite EIF Equations*

Equations (29a) and (29b) are fairly complex and require the computation of gradients for several terms and/or groups of terms. This complexity is due to the inclusion of the high-order ε terms, which are required to extend the approach to moderate Mach numbers. Many flows of practical interest, however, are characterized by low Mach numbers. For such flows, low-order equations, such as $\mathcal{O}(\varepsilon^2)$ and $\mathcal{O}(\varepsilon^4)$, may provide sufficiently accurate solutions at significantly reduced computational cost and code complexity. To investigate this, the

$\mathcal{O}(\varepsilon^2)$- and $\mathcal{O}(\varepsilon^4)$-composite EIF equations have been applied to the spinning vortex pair and shear layer problems described above.

The acoustic fields for the spinning vortex pair have been computed at three different rotating Mach numbers, $M_r = 0.05$, $M_r = 0.10$, and $M_r = 0.20$, which correspond to vortex circulations of $\Gamma = 0.628$, $\Gamma = 1.257$, and $\Gamma = 2.513$, respectively. The peak Mach numbers for these cases are 0.125, 0.25, and 0.50. Figure 3 shows the difference between the acoustic density fields computed with the baseline and $\mathcal{O}(\varepsilon^2)$-equations for each M_r. The difference range (i.e., the difference in $\Delta\rho'$, where $\Delta\rho' = \rho'_{\max} - \rho'_{\min}$) listed on these figures excludes the range associated with the small circular region of radius $16r_o$, centered in the computational domain. The relatively large differences in this region are believed to be due to different resolution of the near-field compressibility of the flow (e.g., the near-field density

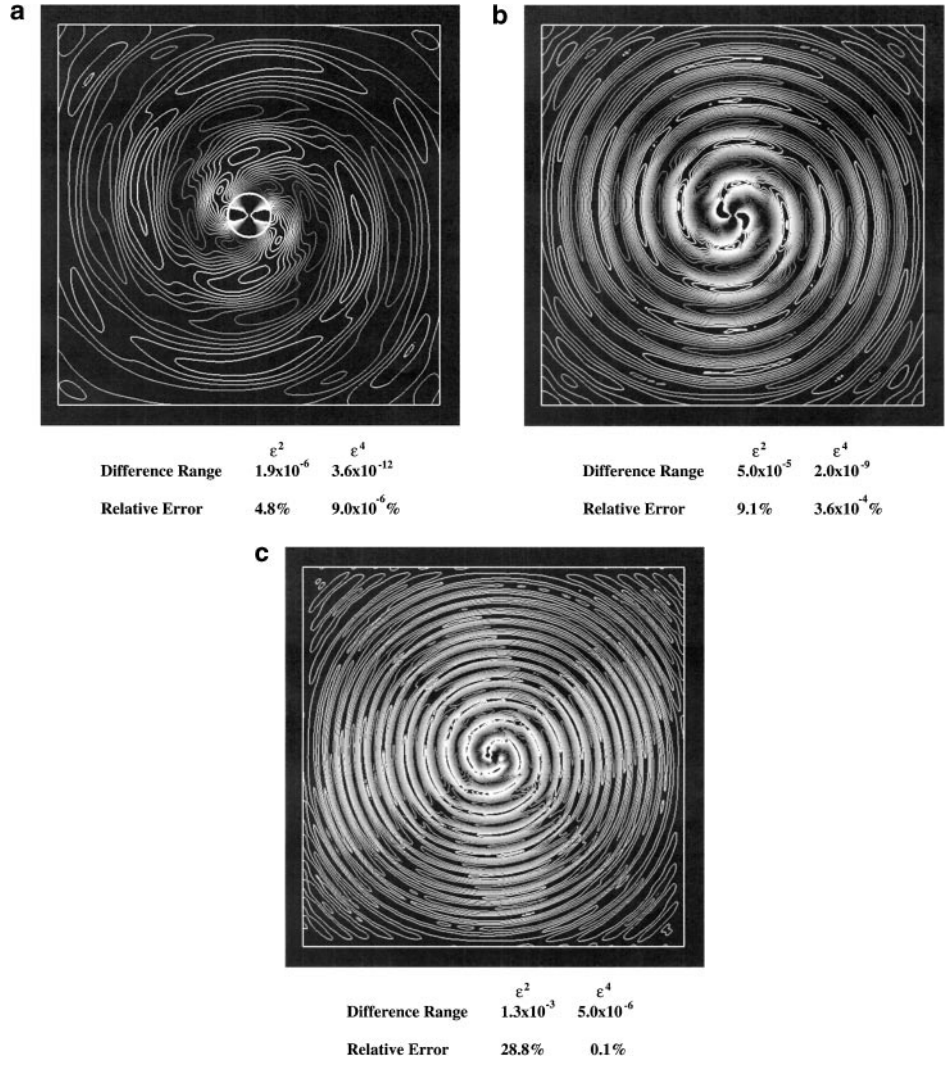

FIG. 3. Spinning vortex pair—difference between computed density fields using the baseline and ε^2-equations. (a) $M_r = 0.05$. 20 contour levels are shown between -1.5×10^{-6} and 1.5×10^{-6}; a circle with radius $16r_o$ is shown centered on the origin. (b) $M_r = 0.10$. 20 contour levels are shown between -5.0×10^{-6} and 5.0×10^{-6}. (c) $M_r = 0.20$. 20 contour levels are shown between -1.5×10^{-3} and 1.5×10^{-3}.

resolved by the $\mathcal{O}(\varepsilon^2)$-equations includes only the first term in the Janzen–Rayleigh expansion of the inner region density, whereas that resolved by the $\mathcal{O}(\varepsilon^4)$-equations includes the first and second terms). As a result, this error does not appear to propagate out to the far field. A measure of relative error can be assessed by considering the ratio of the difference range to the acoustic density field range computed using the baseline equations. This is shown below for computing the relative error associated with the $\mathcal{O}(\varepsilon^2)$-equations,

$$\text{Relative Error} = \frac{(\Delta\rho')_{\varepsilon^2\text{-Eqs.}} - (\Delta\rho')_{\text{Baseline Eqs.}}}{(\Delta\rho')_{\text{Baseline Eqs.}}}. \tag{33}$$

The relative errors have been determined for each M_r and are included in Fig. 3 for both the $\mathcal{O}(\varepsilon^2)$- and $\mathcal{O}(\varepsilon^4)$-solutions (excluding the difference range associated with the circular region described above). The solution obtained with the $\mathcal{O}(\varepsilon^4)$-equations is effectively the same as the solution obtained with the baseline equations. The relative error associated with the $\mathcal{O}(\varepsilon^2)$-equations is seen to increase with increasing Mach number. For $M_r = 0.05$, the relative error was less than 5%, for $M_r = 0.10$, the relative error was approximately 10%, and for $M_r = 0.20$, the relative error was over 25%. Line plots of the difference between the baseline, $\mathcal{O}(\varepsilon^2)$-, and $\mathcal{O}(\varepsilon^4)$-solutions are shown in Fig. 4 along the 45° line from the origin to the upper right-hand side of the computational domain. The range shown in these plots excludes the difference range associated with $r < 16r_o$, consistent with Fig. 3. For comparison purposes, Figs. 4a, 4b, and 4c also include the baseline solution multiplied by scale factors of 0.035, 0.10, and 0.25 for $M_r = 0.05$, 0.10, and 0.20, respectively. These

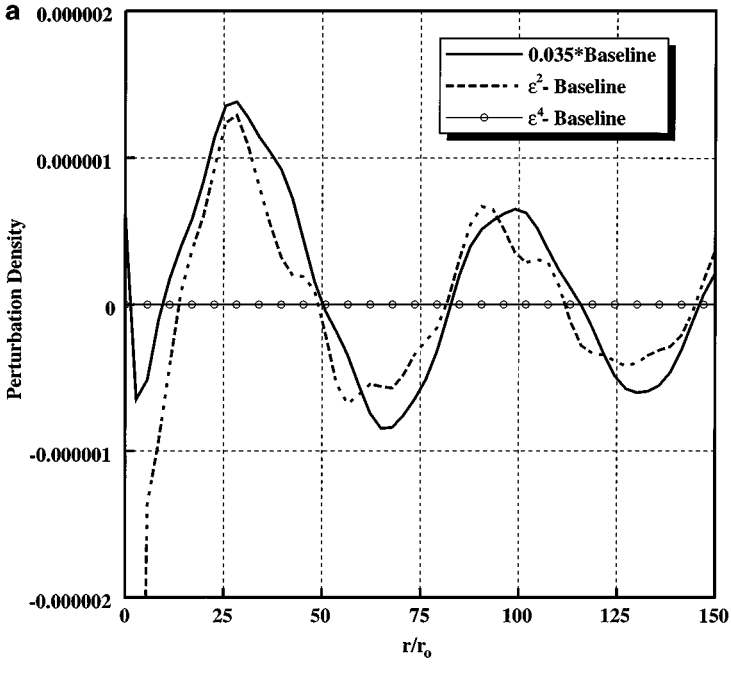

FIG. 4. Spinning vortex pair—differences between solutions of perturbation density along $x_1 = x_2$. Differences are between the solution obtained with the baseline equations and the solutions obtained using the ε^2- and ε^4-equations. (a) $M_r = 0.05$. (b) $M_r = 0.10$. (c) $M_r = 0.20$.

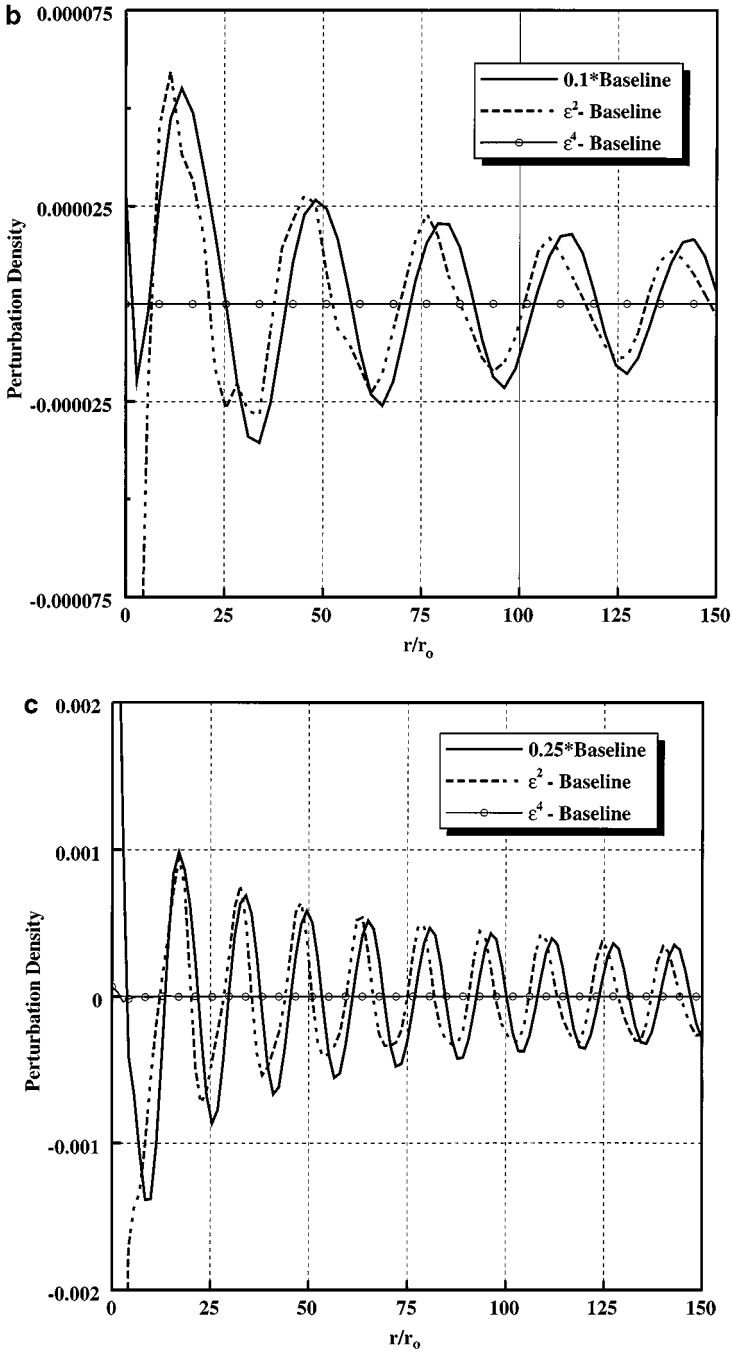

FIG. 4—*Continued*

factors were selected so that the scaled baseline solutions approximately match the amplitude of the difference range of each computed solution over most of the acoustic domain. This provides another measure of the error associated with the $\mathcal{O}(\varepsilon^2)$- and $\mathcal{O}(\varepsilon^4)$-equations relative to the baseline EIF equations and verifies that the relatively large differences seen near the origin do not propagate out to the far field.

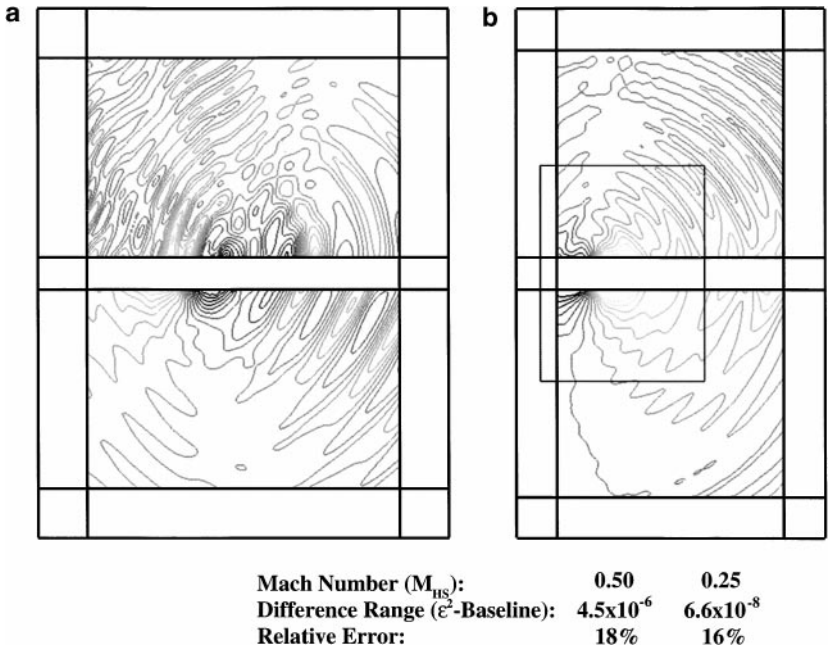

FIG. 5. Planar shear layer—difference between computed density fields using the baseline and ε^2-equations. (a) $M_{\text{HS}} = 0.50$. (b) $M_{\text{HS}} = 0.25$. The square inset in Fig. (5b) is the size of the entire computational domain shown in Fig. (5a).

For the planar shear layer, the acoustic fields have been computed with the $\mathcal{O}(\varepsilon^2)$-, $\mathcal{O}(\varepsilon^4)$-, and baseline composite EIF equations using two-high-speed stream Mach numbers, $M_{\text{HS}} = 0.50$ and $M_{\text{HS}} = 0.25$. In each of these cases, the ratio of low- to high-speed stream Mach numbers was 0.5. Similar to the spinning vortex pair, results using the $\mathcal{O}(\varepsilon^4)$-equations are virtually identical to those using the baseline EIF equations. Figure 5 shows the difference between solutions obtained with the baseline and $\mathcal{O}(\varepsilon^2)$-equations for the $M_{\text{HS}} = 0.25$ and $M_{\text{HS}} = 0.50$ cases. These differences exclude the region of significant non-zero hydrodynamic gradients (i.e., the region excluded in the Fig. 2b acoustic field) for the same reason that the small circular region is excluded in the evaluation of the spinning vortex pair solutions. Consistent with the spinning vortex pair simulations, the relative error with the $\mathcal{O}(\varepsilon^2)$-equations is higher for the higher Mach number case. For $M_{\text{HS}} = 0.25$, the relative error was approximately 16%, and for $M_{\text{HS}} = 0.50$ this error was approximately 18%.

In contrast to the spinning vortex pair problem, the relative error does not provide the best indication of the performance of the $\mathcal{O}(\varepsilon^2)$- and $\mathcal{O}(\varepsilon^4)$-equations as a function of Mach number for the shear layer problem. This is because the amplitude of the acoustic waves at the far field varies significantly with θ, where θ is the angle measured counter-clockwise from the centerline of the shear layer. Therefore, the relative error would not necessarily reflect significant sound pressure level (SPL) differences for low-amplitude waves. A better indication of the performance of the $\mathcal{O}(\varepsilon^2)$-equations for this flow is provided by comparing the computed far-field directivity patterns. Figure 6 shows the directivity patterns using the baseline and $\mathcal{O}(\varepsilon^2)$-equations for both Mach number cases. For the lower Mach number case, little difference (i.e., less than 2 dB) is seen in the solutions computed using the baseline and $\mathcal{O}(\varepsilon^2)$-equations over the entire range of θ. For the higher Mach number case, the basic character of the directivity pattern obtained with the baseline equations was also

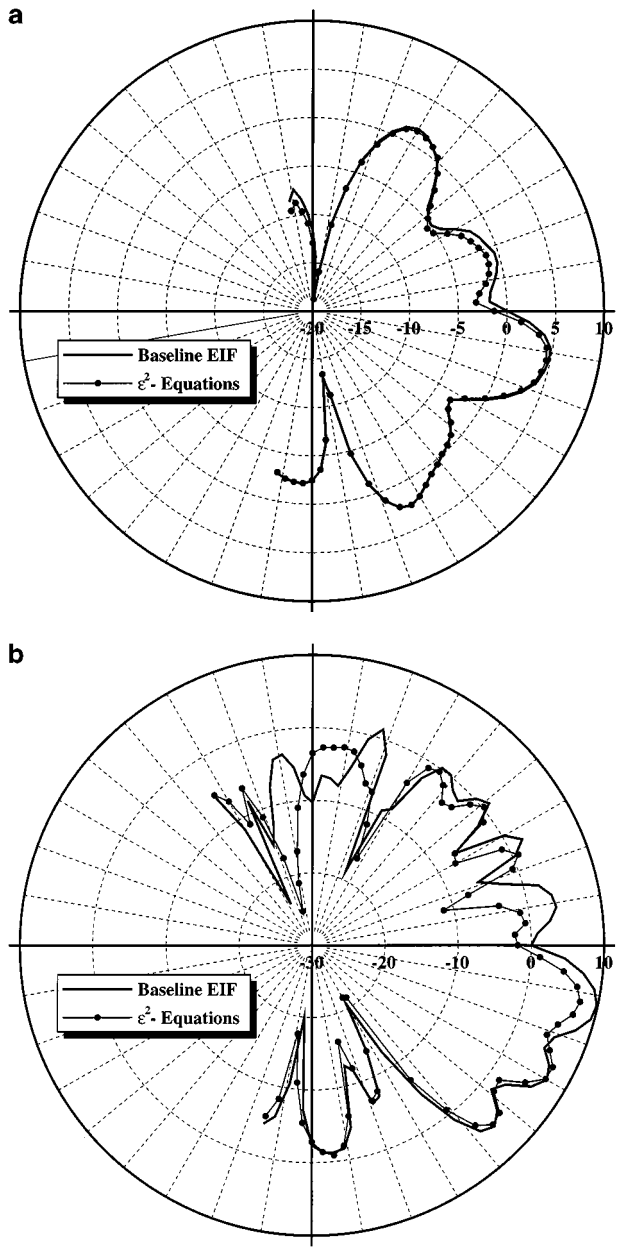

FIG. 6. Planar shear layer—predicted far-field directivity pattern (normalized sound pressure level, dB) obtained using the baseline and ε^2-equations. (a) $M_{\mathrm{HS}} = 0.25$. (b) $M_{\mathrm{HS}} = 0.50$.

obtained with the $\mathcal{O}(\varepsilon^2)$-equations as shown in Fig. 6b. However, significant differences are seen in the high-speed stream side, in particular for waves that propagate upstream into the u_{0i} flow field (i.e., for $\theta > 60^\circ$).

The $\mathcal{O}(\varepsilon^4)$-equations are not significantly simplified as compared to the baseline equations. Because of this, there is little computational advantage in using the $\mathcal{O}(\varepsilon^4)$-equations instead of the baseline equations. For example, use of the $\mathcal{O}(\varepsilon^4)$-equations reduces the computational time by less than 5%. In contrast, the $\mathcal{O}(\varepsilon^2)$-equations are considerably

simplified relative to the baseline equations and result in a 30% reduction in computational time. Furthermore, the $\mathcal{O}(\varepsilon^2)$-equations are significantly easier to implement into a numerical solver. For low Mach number flows, the baseline equations have been shown to offer little improvement over the $\mathcal{O}(\varepsilon^2)$-equations in predicting far-field noise levels and directivity patterns. Because of this, and because of the benefits associated with the simplified form of the $\mathcal{O}(\varepsilon^2)$-equations, these equations are recommended for flows with peak Mach numbers less than approximately 0.25.

C. *Comparison with Acoustic Analogies*

In the previous section, the effects of truncating the EIF equations to lower orders of ε were computationally evaluated using two unsteady flow problems. Some of the benefits of the EIF approach can be demonstrated by comparing the $\mathcal{O}(\varepsilon^2)$-, $\mathcal{O}(\varepsilon^4)$-, and baseline composite EIF equations with the acoustic analogies described previously in this paper. To that end, two modified versions of Eqs. (29) were evaluated. The first modification did not include the flow–acoustic interaction terms or the $\partial(\rho_1 u_{0i} u_{0j})/\partial x_j$ term. The acoustic analogy formulation corresponding to this modification is Lighthill's equation, Eq. (1), with $T_{ij} = \rho_0 u_{0i} u_{0j}$. The second modification consisted of Eqs. (29) without the flow–acoustic interaction terms. Thus, the acoustic analogy formulation corresponding to this modification includes the first compressible correction term (Term I) of Eq. (32). Figure 7 shows the difference between the baseline solution and the solutions obtained with these two modifications for the three spinning vortex pair cases considered earlier. For reference, this figure includes the difference between the baseline and $\mathcal{O}(\varepsilon^2)$-solutions. The first compressible

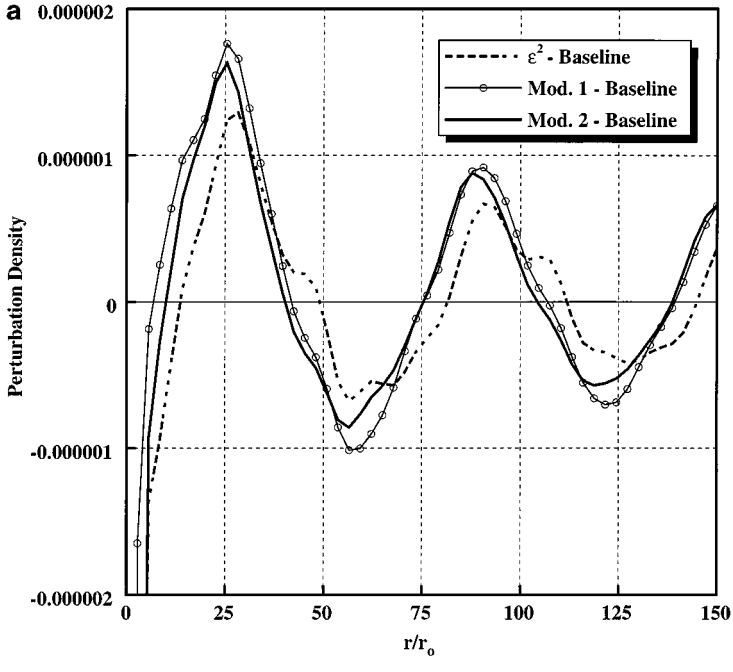

FIG. 7. Spinning vortex pair—differences between solutions of perturbation density along $x_1 = x_2$. Differences are between the solution obtained with the baseline equations and the solutions obtained using the ε^2-, Mod. 1, and Mod. 2 equations. (a) $M_r = 0.05$. (b) $M_r = 0.10$. (c) $M_r = 0.20$.

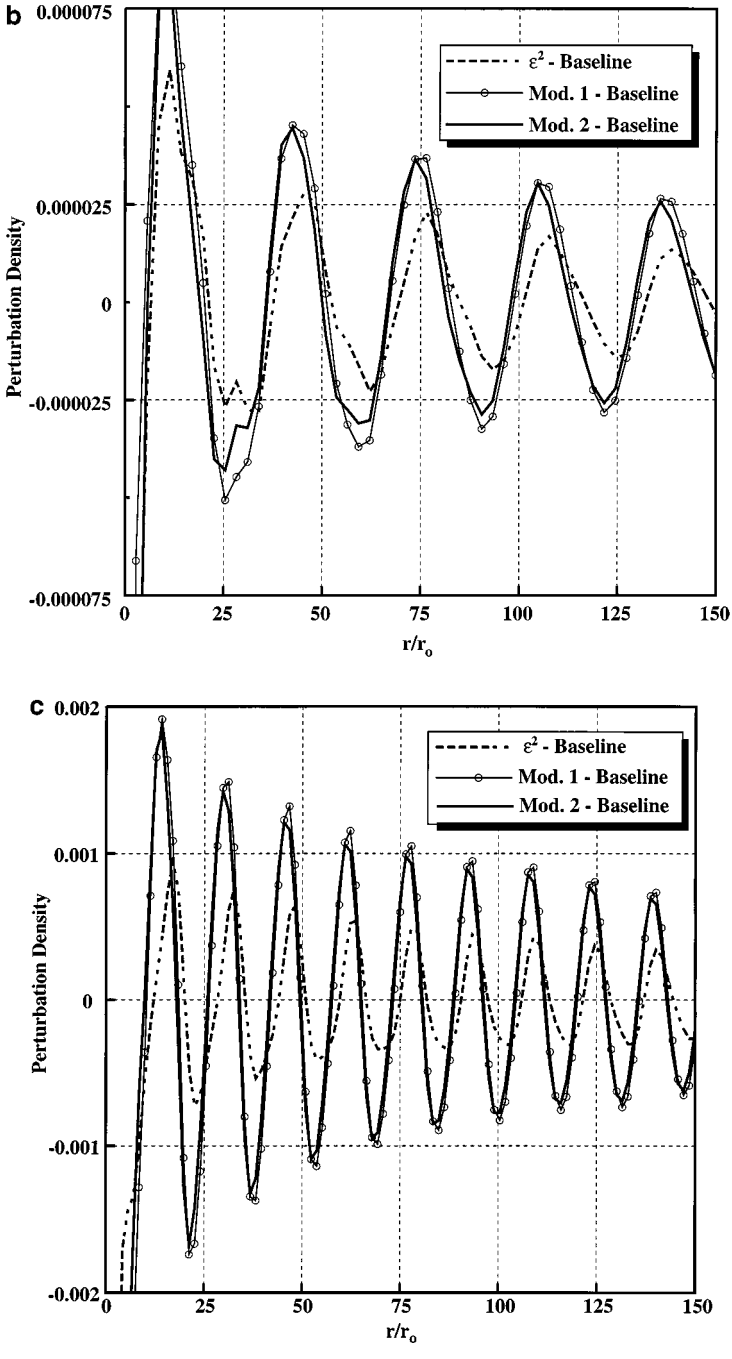

FIG. 7—*Continued*

correction term is seen to have little effect on the solution for all three M_r cases considered. For the $M_r = 0.05$ case, the $\mathcal{O}(\varepsilon^2)$-solution provides little improvement in error relative to the solution obtained with Lighthill's incompressible source term. However, significant improvement is evident for the higher M_r cases (e.g., at $M_r = 0.20$ the error is reduced by a factor of 2).

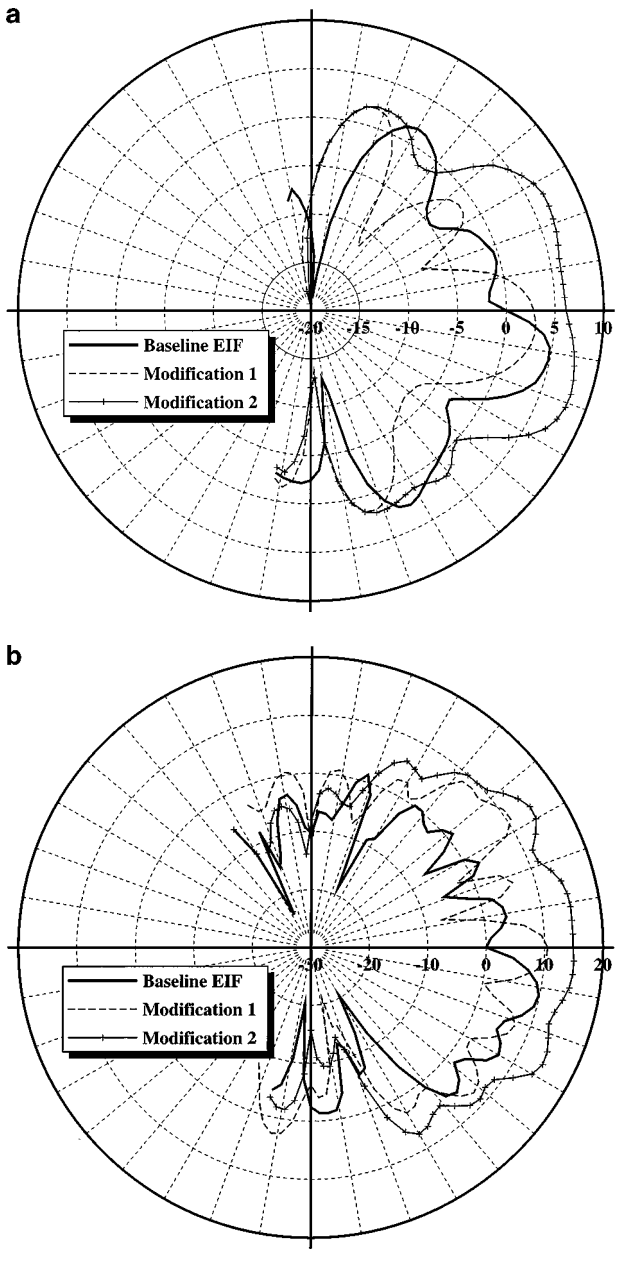

FIG. 8. Planar shear layer—predicted far-field directivity pattern (normalized sound pressure level, dB) obtained using the ε^2-, Mod. 1, and Mod. 2 equations. (a) $M_{\mathrm{HS}} = 0.25$. (b) $M_{\mathrm{HS}} = 0.50$.

The first and second modified forms of Eqs. (29) were also applied to the shear layer problem. Figure 8 shows the directivity patterns for the $M_{\mathrm{HS}} = 0.50$ and 0.25 cases using these modified equations. In addition, this figure shows the results obtained using the baseline EIF equations. Large errors relative to the baseline results are seen using the modified equations and are attributed to the neglect of the flow–acoustic interaction terms. For this flow, which has a large region with significant hydrodynamic velocities and velocity gradients (i.e., a

large Λ as described in Section II-E, the flow–acoustic interaction terms play an important role in the convection and refraction of sound. Acoustic analogies that do not include these terms cannot capture the superdirective character of the acoustic field predicted with DNS and the EIF approach. Of interest is that the second modified equation (i.e., the equation that includes the effects of Term I of Eq. (32)) does not improve the comparison with the baseline EIF equation solution. One explanation for this is that this term is balanced, at least in part, by the flow–acoustic interaction terms that have the same order of ε as Term I.

IV. CONCLUSIONS

A Janzen–Rayleigh expansion of the compressible flow equations has been performed that, to lowest order, describes the low Mach number approximation of a thermodynamic field. Results of the expansion, in conjunction with an additive composition matching procedure, have been used to develop the EIF equations, which have been shown to include an infinite power series in M^2. Relations between the hydrodynamic density and hydrodynamic pressure fields, and between the acoustic pressure, acoustic density, and hydrodynamic density fields, are essential elements in the EIF approach. These relations have been established using the Janzen–Rayleigh expansion.

Two low-order approximations of the baseline EIF equations have been developed. These equations, referred to as the $\mathcal{O}(\varepsilon^2)$- and $\mathcal{O}(\varepsilon^4)$-composite EIF equations, include terms up to order M^2 and M^4, respectively. The $\mathcal{O}(\varepsilon^2)$-, $\mathcal{O}(\varepsilon^4)$-, and baseline composite EIF equations have been tested using two unsteady flow problems, the spinning vortex pair and a forced planar shear layer. The error associated with the use of the lower-order approximations increases with the Mach number. However, both of these approximations have been shown to yield adequate acoustic predictions, as long as the Mach number is below approximately 0.25. The $\mathcal{O}(\varepsilon^2)$-equations require approximately 30% less CPU time than the baseline equations, are much simpler to program, and are therefore recommended for low Mach number ($\mathrm{M} < 0.25$) simulations.

Acoustic analogy formulations of each of the equations (i.e., $\mathcal{O}(\varepsilon^2)$-, $\mathcal{O}(\varepsilon^4)$-, and baseline equations) have also been developed. Each of these formulations includes flow–acoustic interaction terms, which cannot be accounted for using the standard acoustic analogy solution approach. Without these terms, the $\mathcal{O}(\varepsilon^2)$-equation closely resembles Lighthill's acoustic analogy, along with an additional term that is identical to one of the compressibility correction terms due to Ristorcelli. Numerical simulations have shown that without the flow–acoustic interaction terms, the acoustic analogies are not able to predict the highly directional character of subsonic shear layers.

APPENDIX: NOMENCLATURE

c	local speed of sound
C_o	ambient speed of sound
c_p	specific heat
F_i	body force per unit volume
k_∞	reference thermal conductivity
ℓ	inner region length scale

L_∞	reference length scale
M	Mach number
M_r	rotating Mach number
p	pressure
$\bar{p}_n$	nth term in inner region p expansion
p_n	$\varepsilon^{2n}\bar{p}_n$
p_1	hydrodynamic pressure
p'	perturbation pressure, $p' = \sum_{m=2}^{n}\varepsilon^{2m}\bar{p}_m$
$\tilde{p}_1$	time-averaged hydrodynamic pressure
Pr	Prandtl number
q_i	heat flux vector, $\partial(kT)/\partial x_i$
q_{ni}	$\partial(kT_n)/\partial x_i$
q'''	heat release per unit volume
r_o	rotation radius, vortex pair
Re	Reynolds number
t	inner region time
$\hat{t}$	outer region time
T	temperature
$\bar{T}_n$	nth term in inner region T expansion
T_n	$\varepsilon^{2n}\bar{T}_n$
T_∞	reference temperature
T_{ij}	Lighthill's stress tensor
$T_{ij}^{(n)}$	order M^{2n} component of T_{ij}
u_i	velocity vector component in i-direction
$\bar{u}_{ni}$	nth term in inner region u_i expansion
u_{ni}	$\varepsilon^{2n}\bar{u}_{ni}$
u_i'	perturbation velocity vector, $u_i' = \sum_{m=1}^{n}\varepsilon^{2m}\bar{u}_{mi}$
u_∞	reference velocity
Δu	streamwise velocity difference across shear layer
u_{avg}	average streamwise velocity in shear layer
x_i	inner region Cartesian coordinates
$\hat{x}_i$	outer region Cartesian coordinates
δ	shear layer thickness
δ_{ij}	Kronecker delta
ε	perturbation parameter ($\varepsilon^2 = \gamma M^2$)
Φ	dissipation function
γ	specific heat ratio
Γ	circulation
λ	acoustic wavelength
Λ	characteristic length of acoustic source region extent
μ	dynamic viscosity
μ_∞	reference dynamic viscosity
Π_n	pressure–density relation term of order ε^{2n}
ρ	density
$\bar{\rho}_n$	nth term in inner region ρ expansion
ρ_n	$\varepsilon^{2n}\bar{\rho}_n$

ρ_1 hydrodynamic density
ρ' perturbation density, $\rho' = \sum_{m=2}^{n} \varepsilon^{2m} \bar{\rho}_m$
ρ_∞ reference density
τ_{ij} viscous stress tensor

ACKNOWLEDGMENTS

The authors acknowledge funding of this investigation provided, in part, under the Electric Boat Corporation IR&D program managed by Dr. Mark Bennett. In addition, the authors are grateful for the helpful discussions with Dr. Jay C. Hardin regarding several technical aspects of this paper.

REFERENCES

1. M. J. Lighthill, *Report on the Final Panel Discussion on Computational Aeroacoustics*, ICASE Report 92-53, 1992.
2. D. G. Crighton, Computational aeroacoustics for low mach number flows, *Computational Aeroacoustics*, edited by J. C. Hardin and M. Y. Hussaini (Springer-Verlag, Berlin/New York, 1993).
3. C. K. Tam, Computational aeroacoustics: Issues and methods, *AIAA J.* **33**, 1788 (1995).
4. D. G. Crighton, Goals for computational aeroacoustics, in *Computational Acoustics: Algorithms and Applications*. edited by D. Lee, R. L. Sternberg, and M. H. Schultz, Proc. 1st IMACS Symp. on Computational Acoustics (Elsevier, New Haven, CT, 1988), p. 3.
5. M. J. Lighthill, On sound generated aerodynamically. I. General theory, *Proc. R. Soc.* **A211**, 564 (1952).
6. H. S. Ribner, *Aerodynamic Sound from Fluid Dilatations*, UTIA Report 86, AFOSR TN3430, 1962.
7. A. Powell, Theory of vortex sound, *J. Acoust. Soc. Am.* **36**, 177 (1964).
8. M. E. Goldstein, *Aeroacoustics* (McGraw–Hill, New York, 1976).
9. S. C. Crow, Aerodynamic sound emission as a singular perturbation problem, *Stud. Appl. Math.* **49**, 21 (1970).
10. G. M. Lilley, *On Noise from Jets*, AGARD, CP-131, 1974.
11. J. R. Ristorcelli, *A Closure for the Compressibility of the Source Terms in Lighthill's Acoustic Analogy*, ICASE Report 97-44, 1997.
12. J. C. Hardin and D. S. Pope, *A New Technique for Aerodynamic Noise Calculation*, DGLRR/AIAA Paper 92-02-076, 1992.
13. J. C. Hardin and D. S. Pope, Sound generation by flow over a two-dimensional cavity, *AIAA J.* **33**, 407 (1995).
14. D. J. Lee and S. O. Koo, Numerical study of sound generation due to a spinning vortex pair, *AIAA J.* **33**, 20 (1995).
15. M. Van Dyke, *Perturbation Methods in Fluid Mechanics* (Parabolic Press, Stanford, CA, 1975).
16. V. R. Lauvstad, On non-uniform Mach number expansion of the Navier Stokes equations and its relation to aerodynamically generated sound, *J. Sound Vibration* **7**, 90 (1968).
17. F. Obermeier, The application of singular perturbation methods to aerodynamic sound generation, singular perturbations and boundary layer theory, in Lecture Notes in Mathematics, Vol. 594, edited by C. M. Brauner, B. Gay, and J. Mathieu (Springer-Verlag, Berlin, 1977), p. 401.
18. S. H. Reitsma, *Numerical Simulation of Low Mach Number Fluid–Acoustic Phenomena*, Ph.D. thesis, Tufts University, Cambridge, MA, 1994.
19. R. W. MacCormack, *A Numerical Method for Solving the Equations of Compressible Viscous Flow*, AIAA Paper 81-0110, 1981.
20. J.-P. Berenger, A perfectly matched layer for the absorption of electromagnetic waves, *J. Comput. Phys.* **114**, 185 (1994).
21. F. Q. Hu, *On Perfectly Matched Layer as an Absorbing Boundary Condition*, AIAA Paper 96-1664, 1996.

22. S. A. Slimon, M. C. Soteriou, and D. W. Davis, Computational aeroacoustics simulations using the expansion about incompressible flow approach, *AIAA J.* **37** (1999).
23. S. A. Slimon and D. W. Davis, *Computational Prediction of Secondary Flows in Complex Piping Systems*, Advances in Computational Methods in Fluid Dynamics, ASME Fluids Engineering Division (FED), Vol. 196, 1994.
24. S. A. Slimon, D. W. Davis, S. Levinson, M. Krane, G. Richard, D. Sinder, H. Duncan, Q. Lin, and J. Flanagan, *Low Mach Number Flow Through a Constricted Stylized Vocal Tract*, AIAA Paper 96-1734, 1996.
25. S. E. Rogers, D. Kwak, and C. Kiris, Steady and unsteady solutions of the incompressible Navier–Stokes equations, *AIAA J.* **29**, 603 (1991).
26. E.-A. Müller and F. Obermeier, *The Spinning Vortices as a Source of Sound*, AGARD CP-22, 1967, p. 22.1.
27. S. A. Slimon, *Aeroacoustic Computation of Subsonic Flows*, Ph.D. thesis, University of Connecticut, Storrs, CT, 1999.
28. T. Colonius, S. K. Lele, and P. Moin, Sound generation in a mixing layer, *J. Fluid Mech* **330**, 409 (1997).